A multicomponent real-fluid fully compressible four-equation model for two-phase flow with phase change

Ping Yi, Songzhi Yang, Chaouki Habchi, Rafael Lugo

1 A multicomponent real-fluid fully compressible four-equation model for two-phase flow with phase

2 change

3

4 Ping Yi[1,2], Songzhi Yang[1,2], Chaouki Habchi[*1,2], Rafael Lugo[1]

5 [1] IFP Energies nouvelles, 1 et 4 avenue de Bois-Préau, 92852 Rueil-Malmaison, France

6 [2] Institut Carnot IFPEN Transports Energies, 1 et 4 avenue de Bois-Préau, 92852 Rueil-Malmaison,

7 France

8

9 Abstract

10 A fully compressible four-equation model for multicomponent two-phase flow coupled with a real-

11 fluid phase equilibrium-solver is suggested. It is composed of two mass, one momentum, and one

12 energy balance equations under the mechanical and thermal equilibrium assumptions. The

13 multicomponent characteristics in both liquid and gas phases are considered. The thermodynamic

14 properties are computed using a composite equation of state (EoS), in which each phase follows its

15 own Peng-Robinson (PR) EoS in its range of convexity, and the two-phase mixtures are connected

16 with a set of algebraic equilibrium constraints. The drawback of complex speed of sound region for

17 the two-phase mixture is avoided using this composite EoS. The phase change is computed using a

18 phase equilibrium-solver, in which the phase stability is examined by the Tangent Plane Distance

19 (TPD) approach; an isoenergetic-isochoric (UVn) flash including an isothermal-isobaric (TPn) flash is

20 applied to determine the phase change. This four-equation model has been implemented into an in-

21 house IFP-C3D software. Extensive comparisons between the four-equation model predictions,

22 experimental measurements in flash boiling cases, as well as available numerical results were carried

23 out, and good agreements have been obtained. The results demonstrated that this four-equation model

24 can simulate the phase change and capture most real-fluid behaviors for multicomponent two-phase

25 flows. Finally, this validated model was applied to investigate the behaviors of n-dodecane/nitrogen

26 mixtures in one-dimensional shock and double-expansion tubes. The complex wave patterns were

27 unraveled, and the effects of dissolved nitrogen and the volume translation in PR EoS on the wave

28 evolutions were revealed. A three-dimensional transcritical fuel injection is finally simulated to

29 highlight the performance of the proposed four-equation model for multidimensional flows.

30

33

34 1. Introduction

35 Accurate and robust modeling of compressible two-phase flow is crucial for many engineering

36 applications, such as fuel injectors, nuclear reactors, rocket motors, as well as gas turbines and heat

1 pumps (Menter, 1994). The involved two-phase flow maybe subcritical, transcritical or supercritical

2 depending on the pressure and temperature operating conditions. Some subsonic, sonic, or supersonic

3 regions may appear due to shock and expansion waves (Courant and Friedrichs, 1999). Indeed, these

4 phenomena are characterized by the violent variations of local Mach number, the large density

5 gradient across liquid and gas phases, the intense compressibility and gas solubility effects, as well as

6 the phase change and non-ideal thermodynamic properties (Yang et al., 2017). Especially, the phase

7 change adds more complexity to the two-phase flow simulation, such as cavitation, strong shock or

8 flash boiling phenomena. Several numerical models have been developed for the simulation of such

9 two-phase flow, with the numbers of transport equations ranging from three to seven depending on the

10 initial equilibrium assumptions. One of the difficulties in modelling is the physical transfer process

11 taking place across the phases interfaces, such as mass, momentum and heat transfer.

12

13 The most general two-phase flow model is the fully non-equilibrium seven-equation model, in which

14 each phase has its own pressure, velocity and temperature, and is governed by its own set of fluid

15 equations. More precisely, it is based on a fully compressible model composed of three balance

16 equations for the gas phase and three balance equations for the liquid phase, together with a transport

17 equation for the phase volume fraction. Such a non-equilibrium model is built using relaxation

18 methods with finite characteristic time for velocity, pressure, temperature and chemical potential at the

19 phase interface (Baer and Nunziato, 1986, Flåtten and Lund, 2011). Alternatively, the stiff relaxation

20 approaches have been proven to be numerically stable. For instance, the pressure and velocity between

21 two phases can be relaxed instantaneously (Saurel and Abgrall, 1999), and these stiff relaxation

22 procedures have also been applied to the temperature and Gibbs free energy (Habchi, 2015, Zein et al.,

23 2010). The seven-equation model shows great capabilities in describing complex wave patterns and

24 correctly capturing the wave propagation in liquid and gas phases, separately (Andrianov et al., 2003).

25 However, the complexity of implementation in computational fluid dynamics software has limited its

26 extensive use, and simpler models are often preferred.

27

28 In order to simplify the seven-equation model, the reduced five-equation models, in which the

29 mechanical and thermal equilibrium are assumed, have been proposed extensively (Allaire et al., 2002,

30 Kapila et al., 2001, Murrone and Guillard, 2005, Saurel et al., 2009). Kapila et al. (2001) have

31 constructed the most popular formulation with two mass conservation equations for the liquid and

32 vapor, one mixture momentum equation, one mixture energy equation, together with a transport

33 equation for the liquid volume fraction. It has been demonstrated that this model shows excellent

34 resolution of interfaces between two compressible fluids (Murrone and Guillard, 2005, Petitpas et al.,

35 2007). However, serious numerical oscillations have been observed due to the non-conservative

36 feature of liquid volume transport equation in this five-equation model. Some other simplified two-

1   phase flow models derived from the above general seven-equation model by assuming zero relaxation

2   time have been proposed and developed (Ransom and Hicks, 1984, Troshko and Hassan, 2001), and

3   the details of these models are summarized in the work of (Zein et al., 2010).

4

Nomenclature			
a, b	Coefficients in PR EoS	ψ	Phase molar fraction
A, B	Coefficients in PR EoS	ϕ	Fugacity coefficient
$C_{s,p}$	Speed of sound for each phase	ε	Tolerance
$C_{s,mix}$	Speed of sound for two-phase	Δt	Time-step
C_p	Isobaric heat capacity	*Superscript*	
e	Internal energy	$*$	Specified constant values in UVn flash
f_k	Fugacity	"	Non-equilibrium values from flow-solver
f_a	Positive real number	L	Laminar
$F_{1,2,3,4}$	Objective functions	T	Turbulent
J	Flux in control volume	*Subscript*	
k	Binary interaction coefficient	p	Phase index
K	Equilibrium factor	k	Species index
$\dot{m}$	Phase change mass rate	mix	Mixture
M	Molecular weight	N	Total number of species
n_k	Mole number of species	g	Gas
R	Universal gas number	l	Liquid
T	Temperature	L	Left
t	Time	R	Right
P	Pressure	0	Initial values
Pr	Prandtl number	*Abbreviation*	
q	Conduction heat flux	CFL	Courant-Friedrichs-Lewy
u	Velocity	C_{12}	N-dodecane
U_F	Front velocity of evaporation wave	EoS	Equation of state
U_L, U_R	Initial conditions	H_2O	Water
V	Molar volume	MM	Multicomponent in both liquid and gas
x,y	Compositions in liquid and gas phase	$NASG$	Noble-Abel-Stiffened Gas
Y	Mass fraction	N_2	Nitrogen
z	Feed ($z_k = n_k/\sum n_k$)	PR	Peng-Robinson
Z	Compressibility factor	$QSOU$	Quasi Second Order Upwind
Greek letters		SG	Stiffened Gas
α	Phase volume fraction	SM	Single component in liquid phase,
ρ	Density		and multicomponent in gas phase
τ	Stress tensor	TPD	Tangent Plane Distance
λ	Heat conductivity	TPn	Isothermal-isobaric flash
μ	Dynamic viscosity	UVn	Isoenergetic-Isochoric flash
ω	Acentric factor	$1D, 3D$	One-, three-dimension

5

Three and four-equation models are also very prevalent and have been widely used to simulate the cavitating flows (Habchi et al., 2008, Kunz et al., 2000, Moreau et al., 2004, Venkateswaran et al., 2002). Four-equation models are composed of three conservation laws for mixture quantities (mass, momentum, energy) in addition to eventual partial density transport for multicomponent problems, along with a phase change source term in the right-hand side. Four-equation models have been proven to show high numerical efficiency (Battistoni et al., 2014). However, the main difficulties of this kind of model are to estimate the mass source term of phase change and the tunable parameters for the evaporation and condensation processes (Utturkar et al., 2005). Recently, (Saurel et al., 2016) proposed a new four-equation model, in which each phase is compressible and the two phases share common pressure, velocity, temperature, and Gibbs free energy. Moreover, a specific phase equilibrium-solver by applying the Noble-Abel-Stiffened Gas equation of state (Le Métayer and Saurel, 2016). Indeed, this fitted-parameters NASG EoS is used to simplify the thermodynamic computations. Distinct advantages of this four-equation model in conjunction with the phase equilibrium-solver have been shown in computational efficiency and numerical stability. It is worth noting that, this phase equilibrium-solver with NASG EoS is currently limited to the liquid phase only with single-component (i.e., gas solubility in liquid phase is neglected). In reality, however, substantial amount of gas dissolved in liquid phase under high pressure conditions makes primary influence on the nucleation and phase change in several industrial devices. Therefore, the full multicomponent real-fluids characteristics need to be considered.

The cubic equation of state (EoS) is well known to be able to capture the real-fluid behaviors for two-phase flow. The non-linearity of real-fluid may cause spurious pressure oscillations if it is not properly resolved (Banuti, 2015). Besides, the squared sound speed predicted by the cubic EoS (e.g., van der Waals) may become negative inside the spinodal region (see Fig. 1), which results in a loss of hyperbolicity (Menikoff and Plohr, 1989, Petitpas et al., 2009). Both Peng-Robinson (PR) (Peng and Robinson, 1976) and van der Waals EoSs belong to cubic EoSs holding the same repulsive term, and the PR EoS only improves the attractive term. Therefore, they hold similar fundamental properties. Even though (Menikoff and Plohr, 1989) only demonstrated the loss of hyperbolicity for van der Waals EoS for instance, the PR EoS holds the same drawback, which has been demonstrated by many scientific materials (Ma et al., 2017, Petitpas et al., 2009, Saurel et al., 2016, Saurel et al., 2017). All these fundamental drawbacks have limited the extensive applications of cubic EoSs.

Recently, the PR EoS has been used to simulate fuel injection processes, but mostly for the simulation of dense-gas or dense-liquid without phase change (i.e., transcritical conditions). For instance, the PR EoS and Soave-Redlich-Kwong EoS (Soave, 1972) have been used for the cryogenic flows (Schmitt et al., 2009, Terashima et al., 2013). The ECN spray A has also been simulated with the assumption of

transcritical conditions and no phase change (Ma et al., 2017), as well as considering the phase change (Matheis and Hickel, 2018). Most studies, however, only focused on the two- and three-dimensional (2D or 3D) simulations, the complex wave patterns in one-dimensional (1D) tube, up to now, have not been understood clearly with the real-fluid equilibrium-solver. The recent studies in one-dimensional tubes (Chiapolino et al., 2017, Goncalvès and Charrière, 2014, Zein et al., 2010) are mainly focusing on the simulation of water-nitrogen with fitted parameter EoSs, and only consider a single-component in the liquid phase (the dissolved gas is neglected). These studies cannot capture the real-fluid behaviors for multicomponent two-phase flows. Therefore, as a prelude of further 3D applications like diesel and gasoline injection modeling, thorough validations of multicomponent real-fluid two-phase flow model are necessary. This is carried out in the present study based on the 1D shock tube, flash boiling and double-expansion tube cases using *n*-dodecane/nitrogen mixture which are typical surrogates for fuel injection in internal combustion engines.

For the simulation of two-phase subcritical flows, a phase equilibrium-solver is needed, in which the phase numbers, compositions, as well as the temperature and pressure are determined at the maximum entropy state of system. (Qiu et al., 2014) has developed a consistent and efficient phase equilibrium-solver using the PR EoS based on the Lagrange-Eulerian framework of KIVA-3 (Amsden, 1997). Besides, there are many other well developed flash approaches, including the isochoric-isothermal (TVn) flash (Espósito et al., 2000), negative flash (Whitson and Michelsen, 1989) and isoenergetic-isochoric (UVn) flash (Castier, 2009). Among them, the UVn flash is an efficient tool for the phase change computations. Following this flash, the equilibrium pressure, temperature and phase compositions can be determined at the given specified mixture internal energy, volume and mole number of each component. Thereby, the UVn flash is identified as the thermodynamic method that should be applied in real-fluid solvers for the phase change computation under the thermodynamic equilibrium condition.

In this study, a detailed multicomponent real-fluid fully compressible model is presented, and the real-fluid wave patterns for water-nitrogen and *n*-dodecane/nitrogen mixtures are unraveled. The structure of this paper is as follows: Section 2 introduces the governing equations, a composite EoS, the numerical method, the hyperbolicity of two-phase Euler system, as well as the primary calculation steps. Section 3 provides the comparisons between the present model predictions and other available numerical results (Chiapolino et al., 2017), as well as the experimental measurements in flash boiling cases (Simões-Moreira and Shepherd, 1999). In Section 4, a series of shock and double-expansion tube cases for *n*-dodecane/nitrogen mixture are simulated, and the wave evolutions are unraveled. Section 5 presents a three-dimensional transcritical fuel injection case to highlight the performance of the proposed four-equation model. Finally, the conclusions are summarized in Section 6.

1 2. Numerical models

2 This paper presents a multicomponent two-phase flow model with real-fluid equilibrium-solver, which

3 is designed to be used for Eulerian large-eddy simulations (LES) of industrial two-phase flow

4 configurations (e.g., liquid-fuel injection in internal combustion engines). The model descriptions are

5 organized with the following three aspects. First, we introduce the governing equations of this model.

6 Then, the numerical methods are described, separately identifying the equations and unknowns in the

7 flow- and equilibrium-solvers, and highlighting the coupling between them. Finally, the hyperbolicity

8 of Euler system closed by the composite EoS for two-phase mixture is discussed.

9

10 2.1 Governing equations

11 In the two-phase flow system, one cannot fundamentally consider the thermal equilibrium at liquid-gas

12 interface in absence of thermal diffusion (Saurel et al., 2016), therefore, the Navier-Stokes equation is

13 more appropriate for two-phase flow systems. The starting point of this work is a filtered fully

14 compressible multicomponent Navier-Stokes equations, including the balance equations for distinct

15 species in gas and liquid phases, mixture momentum, and mixture specific internal energy as follows:

16
$$\frac{\partial \alpha_g \rho_{k,g}}{\partial t} + \frac{\partial \alpha_g \rho_{k,g} u_i}{\partial x_i} = \dot{m}_k \tag{1}$$

17
$$\frac{\partial \alpha_l \rho_{k,l}}{\partial t} + \frac{\partial \alpha_l \rho_{k,l} u_i}{\partial x_i} = -\dot{m}_k \tag{2}$$

18
$$\frac{\partial \rho u_i}{\partial t} + \frac{\partial \rho u_i u_j}{\partial x_j} = \frac{\partial P}{\partial x_i} + \frac{\partial \tau_{ij}^{LT}}{\partial x_j} \tag{3}$$

19
$$\frac{\partial \rho e}{\partial t} + \frac{\partial \rho e u_j}{\partial x_j} = -P \frac{\partial u_j}{\partial x_j} - \frac{\partial q^{LT}}{\partial x_j} + \tau_{ij}^{LT} \frac{\partial u_i}{\partial x_j} \tag{4}$$

20 As long as the multicomponent mixture is outside the vapor dome (i.e., single phase), the above

21 system is closed by PR EoS (Eqs. (5)). However, if the mixture is inside the vapor dome (i.e., two

22 phase), the system is closed by the composite EoS connected with the set of algebraic equations (Eqs.

23 (5) and (6)). This thermodynamic closing is inspired and very similar to the one used in the two-phase

24 flow models of (Saurel et al., 2008), (Petitpas et al., 2009), (Wareing et al., 2013), and (Saurel et al.,

25 2016), except for different EoSs used for each phase. In addition, in the composite EoS, each phase

26 always follows its own PR EoS, and the equilibrium connection constraints (Eqs. (6)) ensure that the

27 mixture speed of sound is always defined.

28
$$\begin{cases} P = \frac{RT}{V_p - b_p} - \frac{a_p \alpha_T}{V_p(V_p + b_p) + b_p(V_p - b_p)}, (p = 1: \text{gas}; p = 2: \text{liquid}) \\ C_{s,p}^2 = \left.\frac{\partial P}{\partial \rho_p}\right|_S = \left.\frac{\partial P}{\partial \rho_p}\right|_T + \frac{T}{C_{v,p}\rho_p^2}\left(\left.\frac{\partial P}{\partial T}\right|_{\rho_p}\right)^2 \end{cases} \tag{5}$$

29
$$\begin{cases} \rho = \sum \alpha_p \rho_p \\ e = \frac{1}{\rho}\sum \alpha_p \rho_p e_p \\ \frac{1}{\rho C_{s,mix,W}^2} = \sum \frac{\alpha_p}{\rho_p C_{s,p}^2} \end{cases} \tag{6}$$

where $\rho_{k,p}$ denotes the partial density of species k in phase p, $p = 1$ for gas (index g) and $p = 2$ for liquid (index l); $k \in [1, N]$, and N is total species number; α_p (with the saturation constaint $\sum \alpha_p = 1$), ρ_p, e_p and $C_{s,p}$ are the phase volume fraction, density, specific internal energy, and speed of sound, respectively; ρ, e, P, T, u and $C_{s,mix,W}$ are the mixture density, specific internal energy, pressure, temperature, velocity and Wood speed of sound (Wood, 1930), respectively (i.e., possible slip velocity between gas and liquid phases is neglected); R is the universal gas constant; $\dot{m}_k$ is the phase change mass rate of species k, which will be determined by the isoenergetic-isochoric flash, described in Appendix A.3. In this model, the species diffusion flux is not considered, and the heat conduction flux is calculated based on the Fourier's law as $q_j^{LT} = -\lambda^{LT} \nabla T$; λ^{LT} is the heat conduction coefficient covering laminar and turbulent contributions, written as $\lambda^{LT} = \lambda^L + K^T \lambda^T$, where $K^T = 1$ for turbulent flows. The laminar contribution λ^L is computed by (Chung et al., 1988) correlation, and the turbulent one is estimated using a given turbulent Prandtl number, $Pr_t = 0.9$. The viscous stress tensor is composed of laminar and turbulent contributions and written as $\tau_{ij}^{LT} = \tau_{ij}^L + K^T \tau_{ij}^T$. As described in our previous work (Habchi, 2015), a Boussinesq approximation is used to compute τ_{ij}^{LT}, for which a subgrid-scale turbulent viscosity given by Smogorinsky LES model is adopted, and the laminar viscosity is computed from (Chung et al., 1988) correlation.

In the above system ((1) – (6)), there are three related volumes, including the mixture molar volume, phase molar volume, and partial volume ($V, V_p, V_{k,p}$). The mixture molar volume is determined by the phase volume as $V = \sum \varphi_p V_p$, where φ_p is the phase molar fraction. Since a multicomponent mixture is considered in each phase, V_p is estimated based on the van der Waals mixing rule considering the interaction between molecular volume, energy and components. For subcritical two-phase conditions, the PR EoS is first solved based on the liquid phase compositions (x_k) and three roots can be obtained. The smallest positive one is selected as the liquid molar volume (V_l). Then, the PR EoS is solved based on the gas phase compositions (y_k) and the largest one is selected as the gas molar volume (V_g). For single-phase conditions, the PR EoS is solved based on the feed, and only the real positive molar volume is considered. When the phase molar volume is known, the phase density and mixture density are separately calculated by $\rho_p = M_p/V_p$ and $\rho = \sum \alpha_p \rho_p$. Then, the partial density ($\rho_{k,p}$) in Eqs. (1) – (6) is related to the phase density (ρ_p) as $\rho_{k,g} = \rho_g (y_k M_k / \sum y_k M_k)$ and $\rho_{k,l} = \rho_l (x_k M_k / \sum x_k M_k)$, where M_k is the molecular weight of species k.

Since the PR EoS has been demonstrated to underestimate the liquid hydrocarbon density, a volume translation method ($V = V + V_{correct}$) has been used for improving the prediction of liquid density like (Baled et al., 2012, Tapriyal et al., 2012). The volume correction ($V_{correct}$) is defined as:

$$V_{correct} = A + BT_r \tag{7}$$

where T_r is the reduced temperature ($T_r = T/T_c$); A and B are coefficients correlating the molecular weight (M) and acentric factor (ω), formulated as:

$$A, B = k_0 + k_1 \exp\left(\frac{-1}{k_2 M \omega}\right) + k_3 \exp\left(\frac{-1}{k_4 M \omega}\right) + k_5 \exp\left(\frac{-1}{k_6 M \omega}\right) \tag{8}$$

where k_1, k_2, k_3, k_4, k_5 and k_6 are the EoS based constants.

It is worth noting that $\alpha_p \rho_{k,p}$ is transported in our four-equation model, this is different from (Matheis and Hickel, 2018) model, in which partial densities of species (ρY_k) in mixture are transported, where Y_k is the mass fraction of species k. Indeed, the present formulation possesses some advantages, for instance, the knowledge of phase compositions obtained from the flow-solver can be used as initializations for UVn flash, as explained below in Section 2.2.

2.2 Numerical methods

This four-equation model has been implemented into an in-house IFP-C3D code (Bohbot et al., 2009) already including a seven-equation model with SG EoS (Habchi, 2015). IFP-C3D is an unstructured parallel solver with a finite volume formalism on staggered grids. As known, Eqs. (1) – (4) are the fully compressible Navier-Stokes equations with a parabolic nature. Without conduction and diffusion terms, Eqs. (1) – (4) are the Euler system (hyperbolic part). In order to solve Navier-Stokes equations, a fractional step approach is used, which is similar to the one used in (Wang et al., 2014). First, assume no phase change and the right hand side of species transport equations is set as zero, and only solve the flow-solver (Eqs. (1) – (4)) without $\dot{m}_k$ terms. Then, an isolated system without flows into and out of the control volume is assumed, only consider the phase change and solve the phase equilibrium-solver (Eqs. (11) – (14)).

In the flow-solver (Eqs. (1) – (4) without $\dot{m}_k$), The parabolic and hyperbolic parts are solved separately and consecutively based on the time-splitting method in IFP-C3D (Bohbot et al., 2009). The time-splitting begins with an implicit Lagrangian stage, then follows a sub-cycled explicit Eulerian stage. In the Lagrangian stage, a second order implicit differencing is used for parabolic terms in Eqs. (1) – (4). The coupled implicit equations (velocity, pressure and temperature) are solved by SIMPLE algorithm (Patankar, 1980). Then, the obtained solutions are updated by solving the hyperbolic part in the Eulerian stage using a quasi-second-order-upwind (QSOU) explicit numerical scheme. The Minmod slope limiter is used for scalar fluxes, and the Van Leer slope limiter is used for momentum fluxes. In order to make sure the stability of using different TVD (total variation diminishing) schemes for momentum and scalars, simple advection of isolated interface cases have been tested. The results indicate that the combined method with Minmod and Van Leer limiters can get stable results with small oscillations, which are close to the results predicted by the same scheme. Considering the length of article, the compared results are not shown here. The above algorithms used in this study are known

1   to be able to ensure a stable quasi-second-order upwind advection for both scalars and momentum

2   (Bohbot et al., 2009).

3

4   Since this system is closed by the thermodynamic closure as Eqs. (5) – (6), it can yield (*2N+7*)

5   equations, including *2N* species, one momentum, one energy balance equations, two PR EoS, three

6   connection constraints. Indeed, there are (*2N+7*) unknowns that need to be solved, including $\rho_{k,g}$, $\rho_{k,l}$,

7   α_g (and $\alpha_l = 1 - \alpha_g$), e_g, e_l, u, P, ρ and e. After the flow-solver, we can get the equilibrium mixture

8   internal energy and density (e^*, ρ^*) denoted by ($*$), as well as the temporary non-equilibrium variables

9   ($\alpha_g'', \alpha_l'', \rho_{k,g}'', \rho_{k,l}'', e_g'', e_l'', P''$), denoted by (″), from which the temporary non-equilibrium phase

10   compositions can be obtained as $x_k'' = \alpha_l'' \rho_{k,l}'' M_k / \sum \alpha_l'' \rho_{k,l}'' M_k$ and $y_k'' = \alpha_g'' \rho_{k,g}'' M_k / \sum \alpha_g'' \rho_{k,g}'' M_k$.

11

12   Basically, the final equilibrium temperature, pressure, and phase compositions (T, P, x_k, y_k) will be

13   computed in the following phase equilibrium-solver. Then, the phase change mass ($\dot{m}_k$) can be

14   obtained, and the volume fraction and partial densities will be updated as follows:

$$\frac{\partial \alpha_g \rho_{k,g}}{\partial t} = \dot{m}_k \tag{9}$$

$$\frac{\partial \alpha_l \rho_{k,l}}{\partial t} = -\dot{m}_k \tag{10}$$

17

18   The phase equilibrium-solver is mainly composed of an isochoric-isoenergetic (UVn) flash, and the

19   target variables are T, P, x_k, y_k. However, since the phase compositions (x_k, y_k) are not independent

20   variables, the equilibrium-factors and vapor fraction (K_k, ψ_g) are used instead. As long as K_k and ψ_g

21   are known, the phase compositions (x_k, y_k) can be obtained as $x_k = z_k^* / (1 + (K_k - 1)\psi_g)$ and

22    $y_k = z_k^* K_k / (1 + (K_k - 1)\psi_g)$, where z_k^* is the feed determined by inputs. Thus, the number of

23   unknowns in the phase equilibrium-solver is (*N+3*), including T, P, ψ_g and K_k ($k = 1, N$). They are

24   subjected to the following set of (*N+3*) algebraic constraints:

$$e^* = [\psi_g(M_g e_g) + (1 - \psi_g)(M_l e_l)]/\bar{M} \tag{11}$$

$$\rho^* = \bar{M}/[\psi_g(M_g/\rho_g) + (1 - \psi_g)(M_l/\rho_l)] \tag{12}$$

$$f_{k,l}/f_{k,g} = 1 \tag{13}$$

$$\sum_{k=1}^{N}(z_k^*(1 - K_k)/(1 + (K_k - 1)\psi_g)) = 0 \tag{14}$$

29   where $f_{k,p}$ is the fugacity of species *k* in phase *p*; $\bar{M}$ is the mixture molecular weight determined by the

30   feed; the liquid and gas internal energy, density and molecular weight (e_p, ρ_p, M_p) are related to

31   T, P, ψ_g. Clearly, based on the above constraints and initializations provided by the flow-solver, the

32   phase equilibrium-solver can be solved iteratively, using the composite EoS approach. In fact, the

33   constraints of Eqs. (11) and (12) are the same with those of *e* and ρ in Eqs. (6). Eq. (13) expresses the

34   equality of chemical potentials, as explained in Appendix A. 3, and the Eq. (14) is the well-known

1 Rachford-Rice equation which is an additional constraint to the equilibrium-solver as used in (Saha

2 and Carrolls, 1997).

3

4 Indeed, the equilibrium-solver is composed of three parts:

5 (1) Phase stability test: it is performed by the Tangent Plane Distance (TPD) criterion (Michelsen,

6 1982) to test the phase stability. The objective function is Eq. (A. 9), and the inputs include

7 temperature, pressure, feed in the assumed phase (T, P, z_k);

8 (2) Isothermal-isobaric (TPn) flash: it is applied to obtain the equilibrium phase compositions (x_k, y_k),

9 and the objective functions are Eqs. (A. 13) − (A. 14). The inputs are temperature, pressure, feed,

10 initial vapor faction and equilibrium factors $(T, P, z_k, \psi_g'', K_k'')$;

11 (3) Isoenergetic-Isochoric (UVn) flash: it is used to get the equilibrium temperature and pressure (T, P)

12 considering the phase change, and the objective functions are Eqs. (A. 17) − (A. 18). The inputs

13 include the mixture specific internal energy, density, feed, vapor fraction, as well as the initial

14 temperature and pressure $(e^*, \rho^*, z_k, \psi_g, T'', P'')$.

15 The detailed phase equilibrium-solver is described in Appendix A.2 − A.3 to make the whole system

16 clear and simplified.

17

18 For this compressible Navier-Strokes equations, the time-steps Δt_L (lagrangian stage) and Δt_E (Euler

19 stage) are selected automatically at the beginning of each cycle. First, because the convective terms are

20 explicitly sub-cycled, the convection time-step (Δt_E) must satisfy the Courant stability condition.

21 Second, because the parabolic terms are implicitly discretized, there are no stability restrictions, but

22 two temporal accuracy conditions, used for the selection of Δt_L in the implicit Lagrangian step. The

23 first accuracy condition is related to the velocity gradient expressed as $\Delta t_L \leq f_a \Delta x / (u^B - u)$, where

24 f_a is the positive real number of order unity. The second accuracy condition is given in terms of the

25 strain tensor rate and calculated as $\Delta t_L \leq f_r / \left(2\sqrt{\frac{1}{3}(p^2 - 3q)/3} \right)$, where p and q can be found in

26 (Amsden et al., 1989). The convection time-step Δt_E must satisfy the Courant-Friedrichs-Lewy (CFL)

27 condition $(\Delta t_E \leq C_{CFL} \Delta x / (u + C_{s,mix}))$ for the stability as the parabolic part of Navier-stokes

28 equation is solved implicitly. Therefore, to ensure these conditions, the final time-step needs to be

29
$$\Delta t = min \left(C_{CFL} \Delta x / (u + c), f_a \Delta x / (u^B - u), f_r / 2\sqrt{\frac{1}{3}(p^2 - 3q)/3} \right) \qquad (15)$$

30

31 2.3 Hyperbolicity of Euler system with PR-EoS

32 Without considering the conduction, diffusion, and phase change terms, the system Eqs. (1) − (4) can

33 be written in the compact form with corresponding initial conditions when dealing with the Riemann

34 problem as

$$\begin{cases} \frac{\partial U}{\partial t} + \frac{\partial F(U)}{\partial x} = 0 \\ U(x,0) = \begin{cases} U_L & if \ x \leq 0.5 \\ U_R & if \ x > 0.5 \end{cases} \end{cases} \qquad (16)$$

where $U = [\alpha_g \rho_{k,g}, \alpha_l \rho_{k,l}, \rho u, \rho e]^t$ are dependent variables, and $F(U) = [\alpha_g \rho_{k,g} u, \ \alpha_l \rho_{k,l} u, \rho u^2 + P, (\rho e + P)u]^t$ presents the associated fluxes; U_L and U_R are the constant initial states in the left (L) and right (R) sides with the discontinuity located at $x = 0.5$. As long as all eigenvalues are real with eigenvectors linearly independent, the system (16) is hyperbolic with *2N+2* (only three distinct) eigenvalues: $u - C_{s,mix}$, u (*2N*-folds) and $u + C_{s,mix}$, where $C_{s,mix}$ is the mixture sound speed (Ma et al., 2017, Menikoff and Plohr, 1989, Petitpas et al., 2009, Saurel et al., 2016). Our Euler system (16) differs only in two aspects from the hyperbolic systems of (Saurel et al., 2016) and (Chiapolino et al., 2017). The main differences appear in: (1) we consider multicomponent in both liquid and gas phases, and (2) we use a composite PR EoS instead of Stiffened Gas EoS.

1) It is well known that our suggested model thermodynamically closed by a cubic equation of state (e.g., PR EoS) is hyperbolic as long as the sound speed is real outside the vapor dome (see (Ma et al., 2017), Appendix B). Here, the vapor dome denotes the region bounded by the bubble curve on left and the dew curve on right, as shown in Fig. 1.

2) However, inside the vapor dome (i.e., two-phase), the issue is complex as the thermodynamic state described by the "mixture PR EoS" is either metastable or unstable/non-convex (see Fig. 1(a)). Here, the "mixture PR EoS" is defined as using the classical PR EoS for two-phase mixtures. Inside the unstable/non-convex region bounded by the spinodal curves ($(\partial P/\partial v)_T = 0$, see Fig. 1(a)), there is a complex speed of sound (SoS) region where the hyperbolicity of Euler system is lost, as depicted by Fig.27 in (Ma et al., 2017). It is therefore not appropriate to use the "mixture PR EoS" to close the Euler system (16). Instead, a "composite EoS" formulation (see Eqs. (5) – (6)) is used as the thermodynamic closure of the two-phase Euler system (16).

In our approach, each phase always has its own PR EoS, and the two-phase mixture state is obtained by a "composite EoS" formulation. Each PR EoS is thermodynamically consistent (convex) with the well-defined speed of sound (see Fig. 1(c) and (d)) outside its corresponding unstable region. The connection between the two phases, being endowed by a "composite EoS", is carried out through a set of algebraic constraints (Eqs. (6) are for the flow solver and Eqs. (11) – (14) are for the equilibrium solver). Unlike the "mixture PR EoS" following a thermodynamic path (see Fig. 1(a)), the Wood sound speed (Wood, 1930) used in the composite EoS only represents the mechanical equilibrium (see Fig. 1(b)), and each phase separately follows its corresponding thermodynamic path as shown in Fig. 1(c) and (d) (Saurel et al., 2008). Due to $C_{s,mix,PR}^2 \neq C_{s,mix,W}^2$, no mixture thermodynamic path is

1 involved when solving the Euler system inside the vapor dome, the mixture speed of sound ($C_{s,mix,W}$)

2 is always defined. This is the reason why the present Euler system can preserve the hyperbolicity

3 inside the vapor dome (Saurel et al., 2008).

4
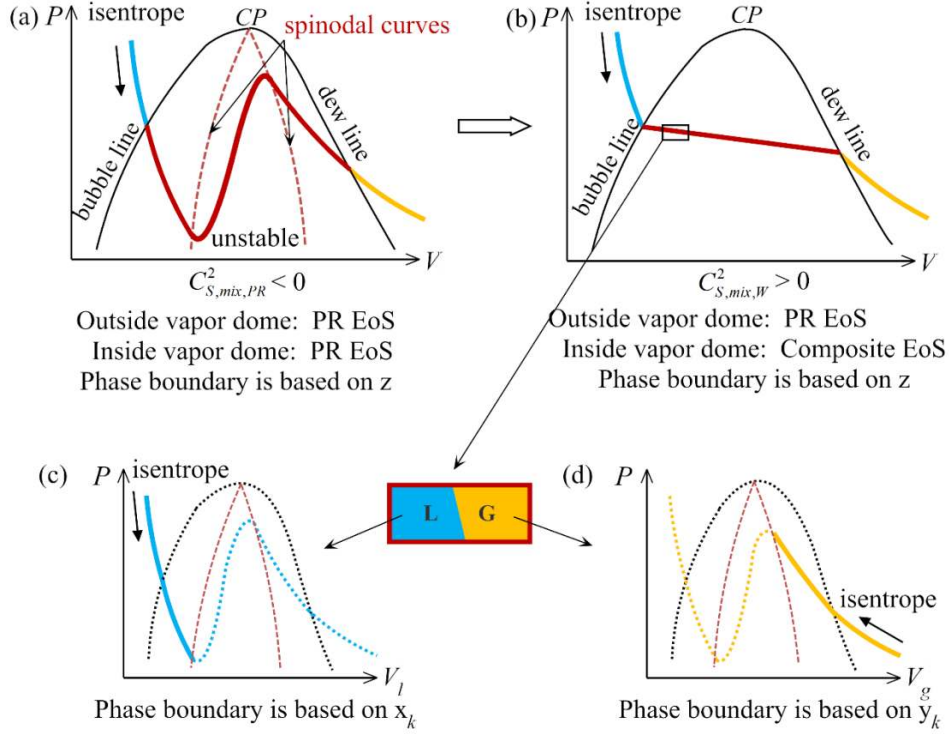
5

6 Fig. 1 Thermodynamic path along an isentrope for multicomponent flow. The vapor dome is enclosed

7 by the bubble and dew lines (a) mixture PR EoS: each phase follows its PR EoS, and the two-phase is

8 described by "mixture PR EoS", the speed of sound is estimated as $C^2_{s,mix,PR} = (\partial P/\partial \rho)_s$, $C^2_{s,mix,PR}$ is

9 negative in the unstable/non-convex region enclosed by spinodal curves ($(\partial P/\partial V)_T = 0$), the phase

10 boundary is depicted based on the feed (z_k); (b) a composite EoS: each phase has its own PR EoS, and

11 the two-phase mixtures are connected by a set of algebraic equations, in which the mixture sound

12 speed is calculated by the Wood formula as $1/(\rho C^2_{s,mix,W}) = \sum_p (\alpha_p/\rho_p C^2_p)$, $C^2_{s,mix,W}$ is always

13 positive inside the vapor dome, the phase boundary is depicted based on the feed (z_k); (c)

14 thermodynamic path along an isentrope for liquid inside the mixture, the phase boundary is depicted

15 based on liquid phase composition (x_k), $C^2_{s,l} = (\partial P/\partial \rho_l)_s$; (d) thermodynamic path along an isentrope

16 for gas inside the mixture, the phase boundary is depicted based on gas phase composition (y_k),

17 $C^2_{s,g} = (\partial P/\partial \rho_g)_s$.

18

19 Based on the studies of (Le Martelot et al., 2014, Lund, 2012, Saurel et al., 2008), it appears that the

20 mechanical equilibrium has the most significant impact on the sound speed, while the thermal and

21 chemical equilibrium assumptions have a much smaller effect. Therefore, there is no practical need to

22 compute the thermal and thermodynamic mixture speed of sound that is quite complex and

computationally expensive (Saurel et al., 2016). This is the reason why the Wood sound speed is widely used although it has a little deviation from the thermodynamic equilibrium one, as shown by (Le Martelot et al., 2014, Saurel et al., 2016, Saurel et al., 2008), to cite a few. Overall, the consequence is that the composite EoS used in this study is a well compromised choice to keep the suggested Euler system being hyperbolic, while using the PR EoS for each phase under an additional numerical stability condition.

Indeed, since a fractional step approach is used to solve the Euler system, as described in Section 2.2, we have met another issue in the composite EoS: the single phase inside the mixture may be compressed or expanded due to the strong shock and rarefaction strength in the Lagrangian stage and enter into the unstable region. To avoid the squared speed of sound of single phase ($C_{s,p}^2$ given by Eqs. (5)) becoming negative, a numerical stability criteria is added, in which the current cycle is restarted with a smaller time-step (Δt) when $C_{s,p}^2 < 0$ ($p = 1$: gas, $p = 2$: liquid). Therefore, our model is able to deal with metastable states in the lagrangian step of the Euler system solver. In fact, the additional numerical stability criterion has been proved to intervene only in the cases involving very strong shock and rarefaction waves (e.g., cavitation). Future work should develop better numerical scheme for the Euler system, avoiding such fractional step approach.

2.4 Calculation procedure

The four-equation model is solved by a fractional step approach (see Fig. 2), including the following primary steps:

1) Read input parameters, including the temperature, pressure, and mass fraction in gas ($T_0, P_0, Y_{g,0}$);

2) Apply TPD function (see Appendix A.2) to test the phase stability;

3) If TPD = 0 or 1, the mixture is in single-phase (gas or liquid), and the initial compositions are set as feed (z_k). Otherwise, the flow is unstable and initial compositions of each phase ($x_{k,0}, y_{k,0}$) are determined by TPn flash (see Appendix A.3.1);

4) Determine the thermal and transport properties, including the conductivity, viscosity, and the thermodynamic partial derivatives, described in the Appendix A.1;

5) In the flow-solver, assuming no phase change, only solve Eqs. (1) – (4) without $\dot{m}_k$ term based on the SIMPLE algorithm, QSOU scheme, using Van Leer and Minmod limiters. The composite EoS (Eqs. (5) – (6)) is used to compute the thermodynamic properties;

6) After the flow-solver, we can get the mixture specific internal energy and density (e^*, ρ^*), which are constraints for the following phase equilibrium-solver (Eqs. (11) – (14)). The non-equilibrium partial density in each phase ($\rho_{k,p}''$) obtained from the flow-solver is used as the initialization for the phase equilibrium-solver;

7) In the phase equilibrium-solver, assuming no flow and only considering the phase change, apply the TPD function to check the phase stability;

8) If the mixture is in single-phase (TPD = 0 or 1), no phase change is assumed. The temperature and pressure are iterated until the equilibrium state of e^*, ρ^* based on Eqs. (11) – (14) is obtained;

9) Otherwise, for the two-phase mixture (TPD = 2), Eqs. (11) – (14) are iteratively solved to determine the equilibrium temperature and pressure (T, P), as well as the phase compositions (x_k, y_k) considering the phase change, and the details are in Appendix A.3; It is important to note that the sound speed is not needed during the iterative relaxation process.

10) At the end of each iteration of UVn flash, if the given tolerance is satisfied, go to the step (11) directly, otherwise, the TPD test is applied to determine the phase stability again, and go to the step (7) or (8) depending on the new TPD value;

11) Finally, the thermal and transport properties are updated with the equilibrium temperature, pressure, and compositions;

12) Return to step (5) and repeat the above processes for the next time-step.

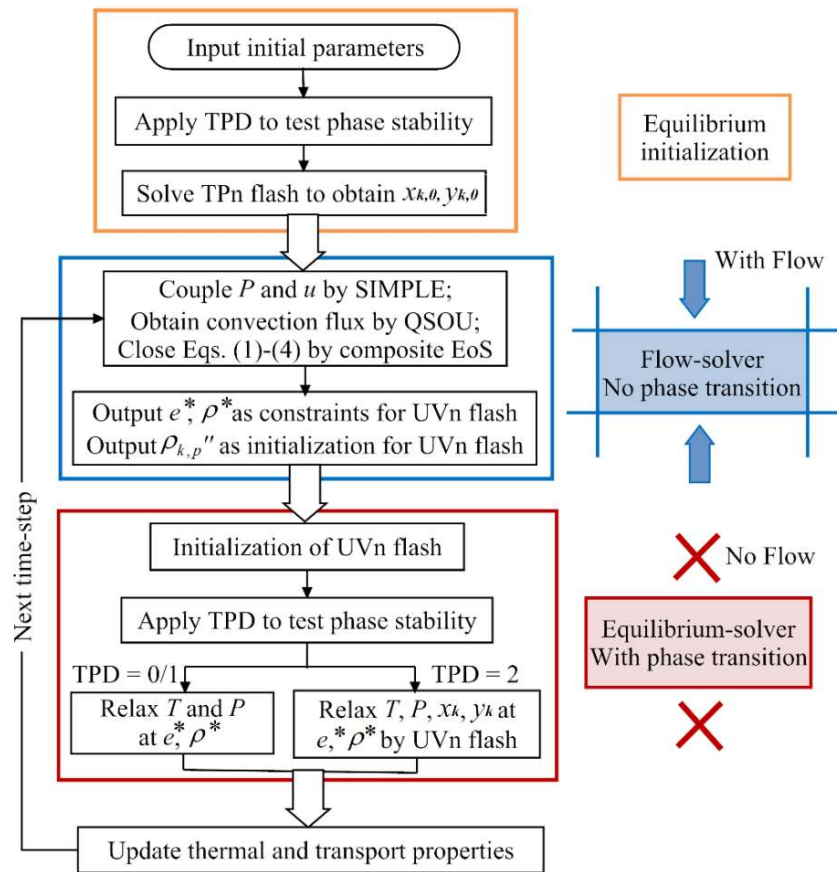Fig. 2Flowchart of the four-equation model with a fractional step approach.

3. Comparison and Validation

This four-equation model is applied to simulate the behaviors of multicomponent two-phase flow in the 1D shock and double-expansion tubes. In Section 3.1, the four-equation model predictions are

compared to the results of (Chiapolino et al., 2017) for shock and double-expansion tubes, followed by Section 3.2, in which flash boiling cases are simulated and the model predictions are validated against experimental measurements (Simões-Moreira and Shepherd, 1999). Section 3.3 illustrates the sensitivity of mesh size, time-step, and convergence tolerance of UVn flash. All cases are simulated using a 1 m long tube and a uniform 1D mesh.

3.1 Comparison with the available numerical results

To evaluate the correctness of implementation, two 1D cases (Table 1) for the water-air mixture separately under shock and double-expansion tube conditions are firstly simulated, and compared with the results of (Chiapolino et al., 2017) model to carry out a qualitative validation. (Chiapolino et al., 2017) model is referred as 4EQ-SM-SG and the four-equation model in this study is termed as 4EQ-MM-PR. For simplicity, the air is replaced by nitrogen (N_2) in this study. In Chiapolino et al. (2017) model, the flow system is similar to our four-equation model, both phases are compressible and assumed in mechanical and thermodynamic equilibrium. However, there are two differences between these two models. The first arises from the multicomponent nature (MM) of our transport equations in liquid phase (Eq. (2)), while the dissolved gas in liquid phase is ignored in Chiapolino et al. (2017) model. Second, the EoSs are different. The Noble Abel Stiffened Gas (NASG) EoS is used in Chiapolino et al. (2017) model to close the governing equations and describe the thermal properties, which have been validated with experimental data in a limited temperature and pressure ranges. Therefore, their results are expected to be very close to the real fluids in these specified ranges, which are valuable as references to verify our implementation qualitatively.

Table 1. Initial parameters for two-phase shock and double-expansion tube cases with water-nitrogen

|	P_L (MPa)	P_R (MPa)	T_L (K)	T_R (K)	u_L (m/s)	u_R (m/s)	$\alpha_{g,L}$ Equilib.	$\alpha_{g,R}$ Equilib.	$Y_{H_2O,L} = Y_{H_2O,R}$ Input
Case 1	0.2	0.1	354	337	0.0	0.0	0.9995744	0.99977	0.3
Case 2	0.1	0.1	293	293	-1.0	1.0	0.9851587	0.98517	0.99998

3.1.1 Results of Case 1

First, a 1D shock tube is simulated (Case 1 in Table 1). The tube is filled with a homogeneous water-nitrogen mixture, and the initial discontinuity is located at 0.5 m. The left side (0.2 MPa) is at a higher pressure than the right side (0.1 MPa). The temperatures in both sides are set the same as those in (Chiapolino et al., 2017). The compared results between the present four-equation and Chiapolino et al. (2017) models at the instant of 1.0 ms are plotted in Fig. 3. It is found that good agreements were obtained in terms of shock wave strength (velocity magnitude), as well as the evolution of pressure and temperature at the contact discontinuity. However, there is a discrepancy in the vapor mass fraction profile as shown in Fig. 3(d). This is because an isothermal-isobaric flash coupled with the PR

EoS is used in this study to estimate the equilibrium vapor mass fraction, which will cause a minor difference with that of Chiapolino et al. (2017) model even though in the same initial temperature, pressure, and feed. In addition, as the dissolved gas in liquid phase is neglected in Chiapolino et al. (2017) model, it will also lead to a negligible deviation in the vapor mass fraction prediction. Even though the vapor mass fraction predicted by these two models are different, their wave evolutions are very similar, and the phase change proportion predicted by these two models are comparable. In this section, we only want to carry out a qualitative comparison to validate our model implementation. Therefore, the reasonable difference between two numerical results can be acceptable.
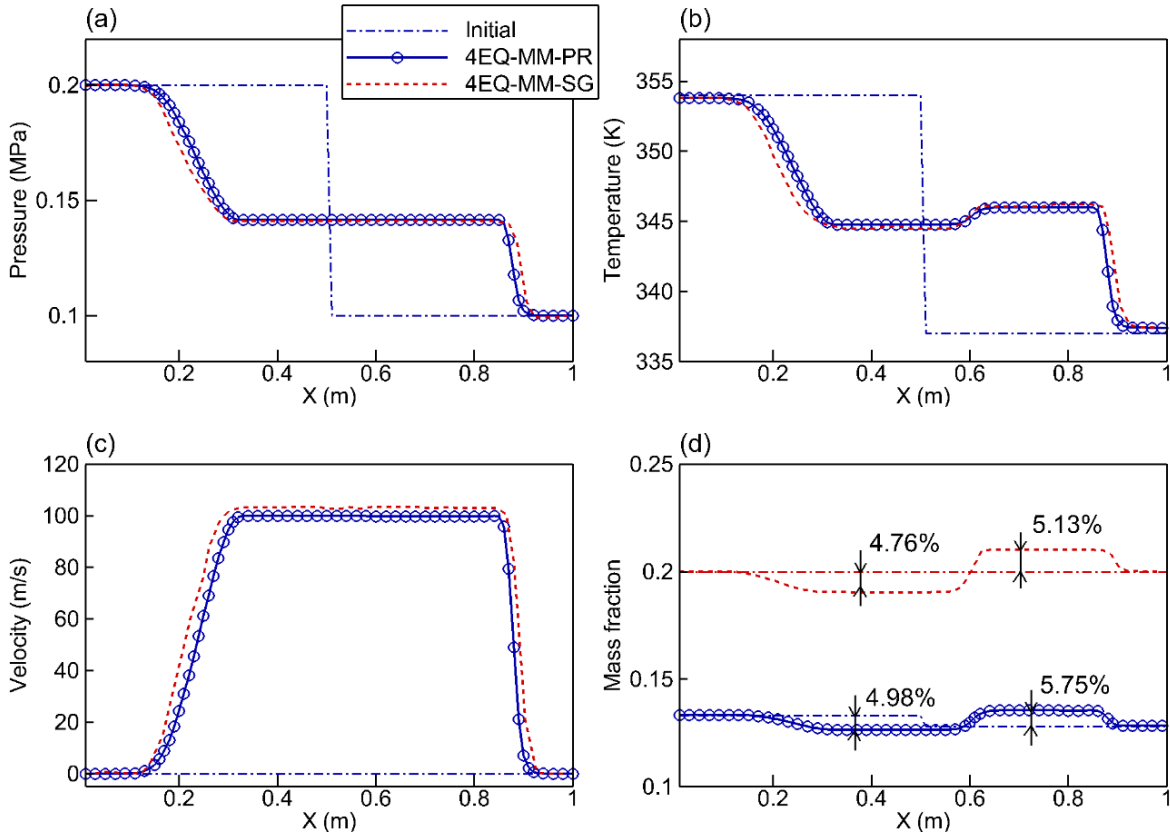
Fig. 3 Compared results between the four-equation (4EQ-MM-PR) and (Chiapolino et al., 2017) (4EQ-SM-SG) models (Case 1: $P_L = 0.2$ MPa, $P_R = 0.1$ MPa, $T_L = 354$ K, $T_R = 337$ K, $\alpha_{g,L} = 0.9995744$, $\alpha_{g,R} = 0.9997698$, $t = 1.0$ ms, thin dash dot lines are initials, 100 cells, CFL = 0.2).

3.1.2 Results of Case 2

The double-expansion tube case also known as cavitation test is performed in a 1 m long tube filled with water combined with a small volume fraction of gaseous nitrogen at atmospheric pressure. The initial discontinuity is set at 0.5 m, and the left and right velocities are -1.0 m/s and 1.0 m/s, respectively.

1   The expansion wave is generated towards to the left side combined with the evaporation front

2   progressing. The compared results between the present four-equation and (Chiapolino et al., 2017)

3   models are presented in Fig. 4. Significant discrepancies are observed in the pressure, temperature and

4   vapor mass fraction predictions between these two models. This is because the dissolved gas in liquid

5   phase is neglected in Chiapolino et al. (2017) model, the equilibrium pressure caused by the expansion

6   wave is equal to the vapor pressure of water. However, in the present four-equation model, the

7   dissolved nitrogen in liquid phase increases the mixture saturation pressure, which qualifies that the

8   final equilibrium pressure with current model is slightly higher than that in Chiapolino et al. (2017)

9   model. On the other hand, since the composite PR EoS is known to underestimate the water density,

10   the temperature is overestimated at the equilibrium state. A more detailed discussion on the influence

11   of liquid density on expansion behaviors is given in Section 4.2.

12
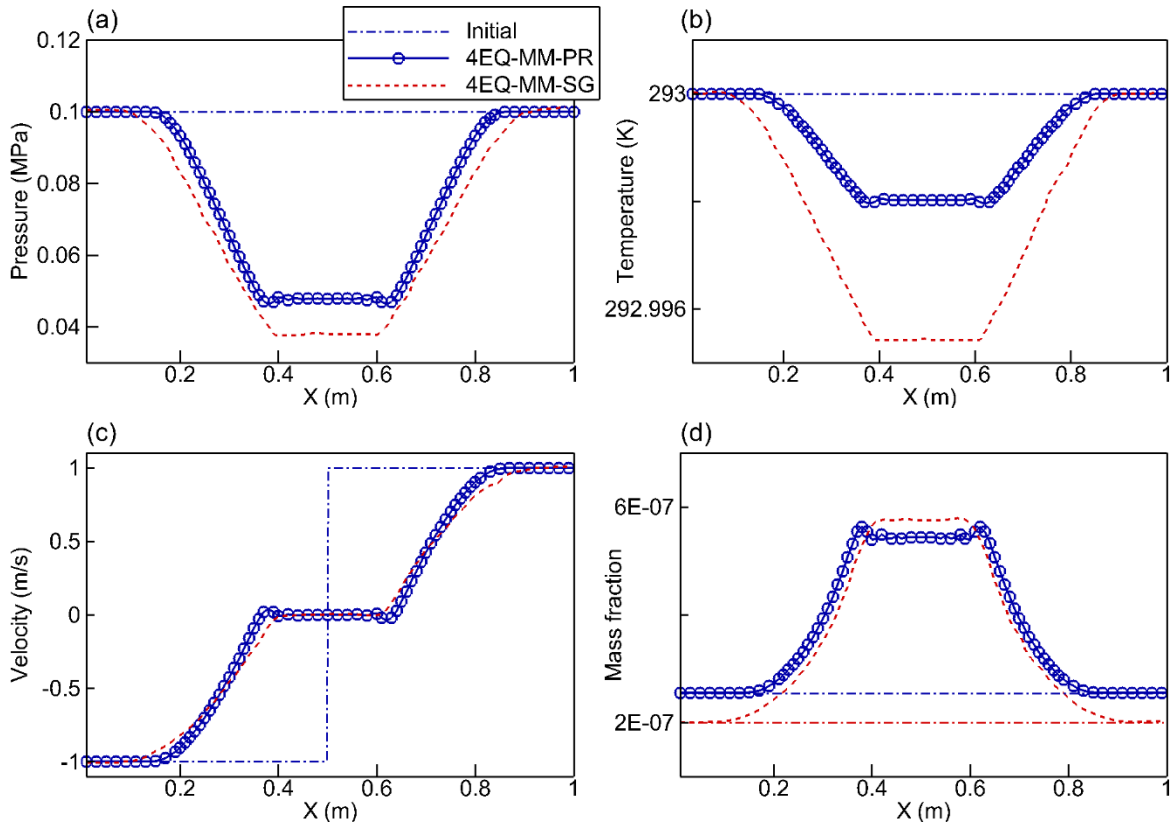
13

14

15   Fig. 4 Compared results between the four-equation (4EQ-MM-PR) and (Chiapolino et al., 2017)

16   (4EQ-SM-SG) models (Case 2: $P_L = P_R = 0.1$ MPa, $T_L = T_R = 293$ K, $\alpha_{g,L} = \alpha_{g,R} = 0.9851587$,

17   $u_L = -1$ m/s, $u_R = 1$ m/s, $t = 3.5$ ms, thin dash dot lines are initials, 100 cells, CFL = 0.2).

18

19   3.2 Flash boiling test cases

20   In order to validate the accuracy of present four-equation model, several flash boiling test cases are

21   simulated and the results are compared with the experimental results (Simões-Moreira and Shepherd,

22   1999). In this flash boiling experiment, a high pressure tube filled with liquid *n*-dodecane at

thermodynamic equilibrium state is connected to a low pressure chamber with gaseous nitrogen, and the detailed parameters of Case 3 are listed in Table 2. The flash boiling has been observed at the liquid-gas interface in the experiment. It has been demonstrated that this kind of flash boiling have similar behaviors with deflagration phenomena in combustion (Kurschat et al., 1992, Thompson et al., 1987). An evaporation front propagates into the liquid side with a steady mean velocity, U_F, which has been measured under various superheated conditions (Simões-Moreira and Shepherd, 1999). In this study, the front velocity, U_F, is estimated based on a simple control volume model and Rankine-Hugoniot equation (Simões-Moreira and Shepherd, 1999), as follows

$$J = (U_F + u_L)\rho_L = (U_F + u_R)\rho_R \tag{17}$$

where u_L and u_R are the fluid velocity of left and right sides, respectively; and J is the superficial mass flux. Since the liquid in left side is stationary ($u_L = 0$), the front velocity can be calculated as

$$U_F = J/\rho_L \tag{18}$$

$$J^2 = (P_L - P_R)/(1/\rho_R - 1/\rho_L) \tag{19}$$

where P_L and ρ_L, as well as P_R and ρ_R refer to the pressure and density before and after the evaporation front, respectively.

Table 2. Initial conditions for flash boiling cases with *n*-dodecane/nitrogen mixture

	P_L (MPa)	P_R (MPa)	T_L (K)	T_R (K)	$u_L = u_R$ (m/s)	$\alpha_{g,L}$ (Equilib.)	$\alpha_{g,R}$ (Equilib.)
Case 3	0.15, 0.22, 0.30, 0.39, 0.50, 0.75, 1.10, 1.30	0.0001	453, 473, 489, 503, 523, 543, 563, 573	543	0.0	0.0001	0.9999

The evaporation front velocities are obtained at several times in the range of 0.2 – 0.4 ms, and the averaged values are compared with the experimental measurements as shown in Fig. 5. It is found that the present model can obtain good agreements with experimental results under low superheated conditions (i.e., less than 503 K). As the superheat degree rises, the discrepancy between experimental results and model predictions increases. Here, the superheat degree is usually defined as the temperature difference between the local temperature and the saturation temperature at a given subcritical pressure. This may be caused by several reasons, including complexities and uncertainties in experiment and assumptions used in the four-equation model. Indeed, unstable interfaces can be observed in experimental images (Fig. 5 in (Simões-Moreira and Shepherd, 1999)) due to the high nucleation rate near phase interface and also at walls. Some small droplets are busted from the interface and flung into the flows, which enhances the gas velocity (u_R). Following (17), the front velocity can be described as $U_F = u_R\rho_R/(\rho_L - \rho_R)$. Due to the increased u_R caused by bursting droplets observed in the experiment, the measured front velocity U_F is enhanced, and the increased extent is growing as the superheat degree rises. Since, however, these effects are neglected in the

1 simulations, the present model underestimates the front velocity at the conditions with high superheat

2 degree. For instance, as the temperature of left side is 573 K, the front velocity is underestimated

3 around 25% as shown in Fig. 5. Therefore, the future work shall include the modelling of the amount

4 of droplets bursting at the interface. Indeed, this phenomenon is important for modeling of gasoline

5 direct injection (GDI) with flash boiling conditions.

6
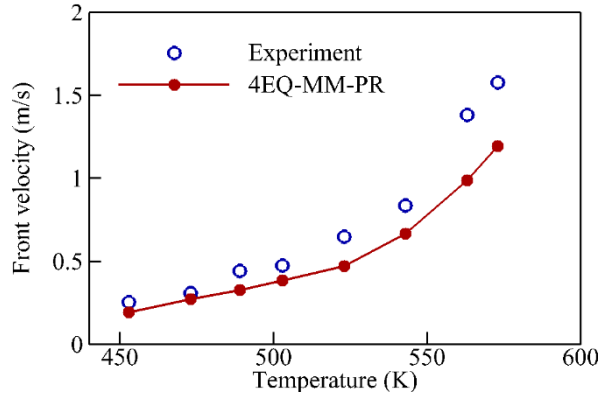
7

8 Fig. 5 Compared evaporation front velocity between experimental results (Simões-Moreira and

9 Shepherd, 1999) and the four-equation model predictions for flash boiling case (Case 3: $P_L = 0.15 -$

10 1.30 MPa, $P_R = 0.0001$ MPa, $T_L = 453 - 573$ K, $T_R = 543$ K, $\alpha_{g,L} = 0.0001$, $\alpha_{g,R} = 0.9999$, $t =$

11 0.2 – 0.4 ms, left side is filled with liquid n-dodecane, right side is filled with gaseous nitrogen).

12

13 The evolution profiles of the flash boiling case with the liquid temperature of 543 K are presented in

14 Fig. 6. Since the evaporation in flash boiling cases takes place within a very thin region, its thickness

15 is quite small in comparison with the fluid length scales. Therefore, there is a sharp discontinuity at the

16 evaporation front (X = 0.5 m) in each profile. In the left side, the pressure drops drastically across the

17 expansion wave, and the superheated liquid is transported along with the evaporation front to the left

18 side at a low speed. The vapor mass fraction increases suddenly to one at the liquid-gas interface.

19 Meanwhile, at the right side, a strong shock wave is produced and propagates towards the low-

20 pressure side. Between the evaporation and shock wave fronts, a simple contact discontinuity (in the

21 range of 0.68 – 0.74 m) is formed to connect the vapor front and shocked gas (Saurel et al., 2008).

22

23 The evolution of fluid velocity and mixture sound speed in different superheated cases are presented in

24 Fig. 7(a) and (b). In this figure, the labels A, B, and C are identified as the evaporated vapor mixture,

25 the contact discontinuity zone behind shock front, as well as the initial nitrogen gas zone, respectively.

26 It is found that the sonic velocity is reached very fast at the evaporation front ($u = C_{s,mix}$), and then

27 the flow evolves to a supersonic regime. In this regime, the vapor velocity increases up to a constant

28 value (at zone B), which increases with raising the superheat degree (see Fig. 7(a)). It is noted that the

29 sound speed at zone A is very low (~ 174.0 m/s), which is consistent with NIST data for gaseous n-

1   dodecane (Linstrom and Mallard, 2001) at the prevailing temperature (~600 K) and pressure (~1 kPa),

2   as can be seen in Fig. 6(a) and (b). Since the fluid temperature at the contact discontinuity is very high

3   (see X ≈ 0.68 − 0.74 in Fig. 6(b)), the corresponding sound speed is very large (see zone B in Fig.

4   7(b)). However, both of them decrease suddenly at the shock front. The detailed wave behaviors are

5   further discussed in the following Section 4.1.2. Based on the above validated results and analysis, the

6   present four-equation model is demonstrated to be able to simulate the complex wave behaviors at the

7   interface with large discontinuities.

8
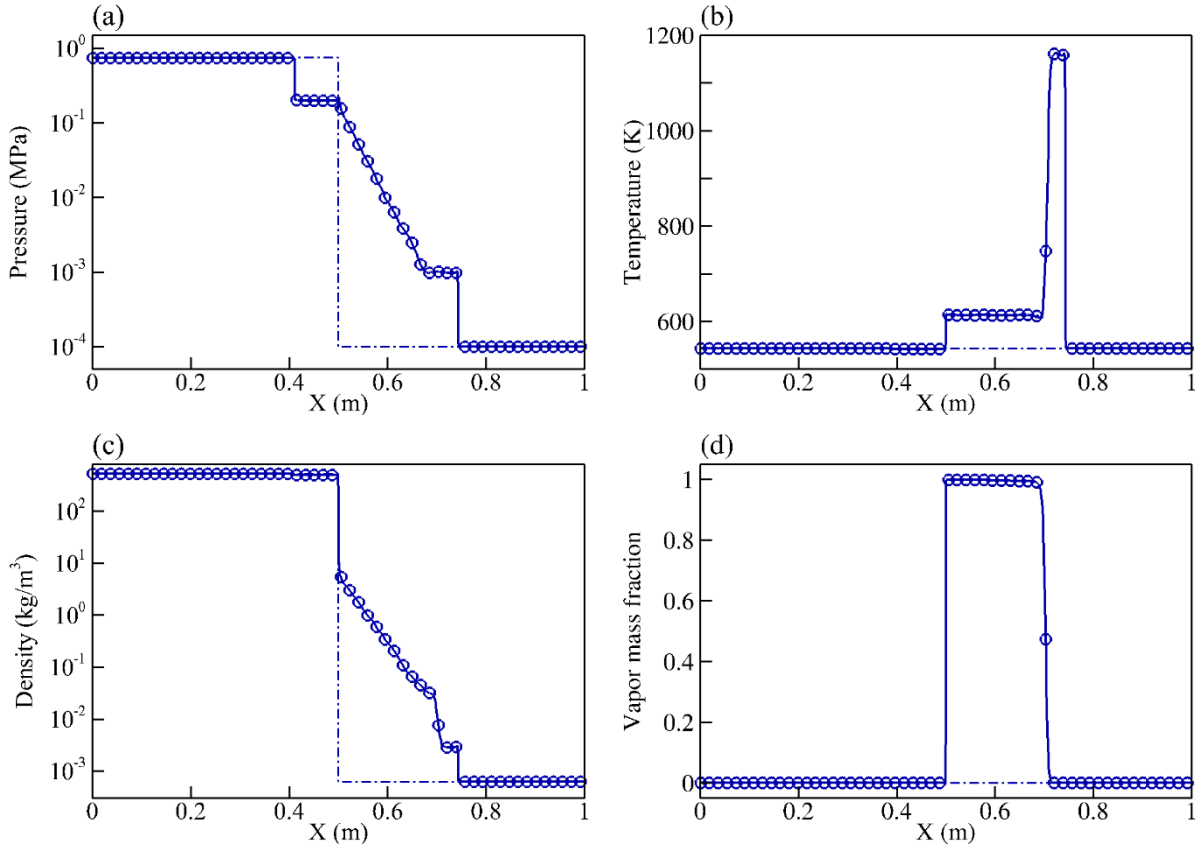
9

10

11   Fig. 6 Wave behaviors of flash boiling case predicted by the four-equation model (P_L = 0.75 MPa,

12   P_R = 0.0001 MPa, T_L = 543 K, T_R = 543 K, $\alpha_{g,L}$ = 0.0001, $\alpha_{g,R}$ = 0.9999, t = 0.2 ms, left side is

13   filled with liquid n-dodecane, right side is filled with gaseous nitrogen, thin dash dot lines are initials).

14
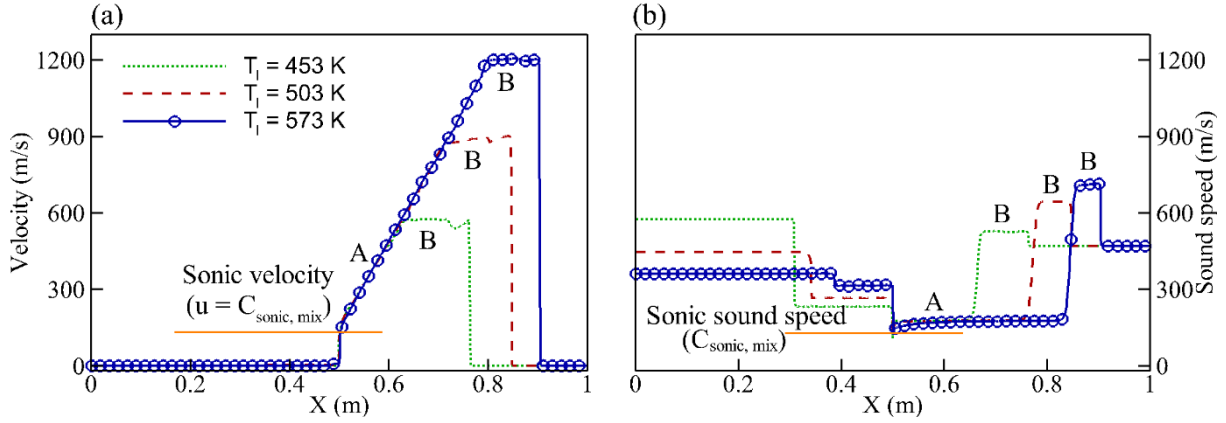
Fig. 7 Fluid velocity and sound speed profiles of flash boiling case predicted by the four-equation model (P_L = 0.15 MPa, T_L = 453 K; P_L = 0.39 MPa, T_L = 503 K; P_L = 1.30 MPa, T_L = 573 K, $\alpha_{g,L}$ = 0.0001, $\alpha_{g,R}$ = 0.9999, t = 0.3 ms)

3.3 Numerical sensitivity analysis

The analysis of mesh size, time-step, and convergence sensitivity is a pre-requisite for the evaluation of the suggested four-equation model accuracy. Several cases have been simulated, and similar behaviors have been obtained. The results of three cases are presented in this section.

3.3.1 Mesh size sensitivity analysis

In order to check the current model in dealing with numerical oscillations, a simple 1D advection of isolated interface case is simulated with Euler equations (Eqs. (1) – (4) without conduction, diffusion and phase change terms) inspired by the work of (Beig and Johnsen, 2015). The tube length is 1 m, the initial temperature and pressure of the whole domain (X $\in$ [0, 1]) filled with n-dodecane and nitrogen are 300 K and 1 bar, respectively. The isolated liquid zone ($Y_{C12H26,l}$ = 0.99) ranging from 0.25 to 0.75 m moves at a constant speed of 100 m/s to the right side. The gas zone is full of the mixture with $Y_{C12H26,g}$ = 0.01. The numerical results depicted in Fig. 8 clearly indicate that our model produces some oscillations in pressure, temperature, and velocity, and these oscillations accumulate with wave propagating. As the mesh is refined, the oscillations are reduced, less than 0.01% with 2000 cells. This corroborates similar results with (Terashima and Koshi, 2012), for instance.

Thereby, we can conclude that the present four-equation model can be used with confidence when the flow gradients are refined appropriately. In the future work, automatic mesh refinement (AMR) will be used with criteria based on density, mass fraction and heat capacity in order to minimize spurious oscillations. More sophisticated approaches like the one of (Pantano et al., 2017) coupled with the PR EoS may be another good option for our future studies.
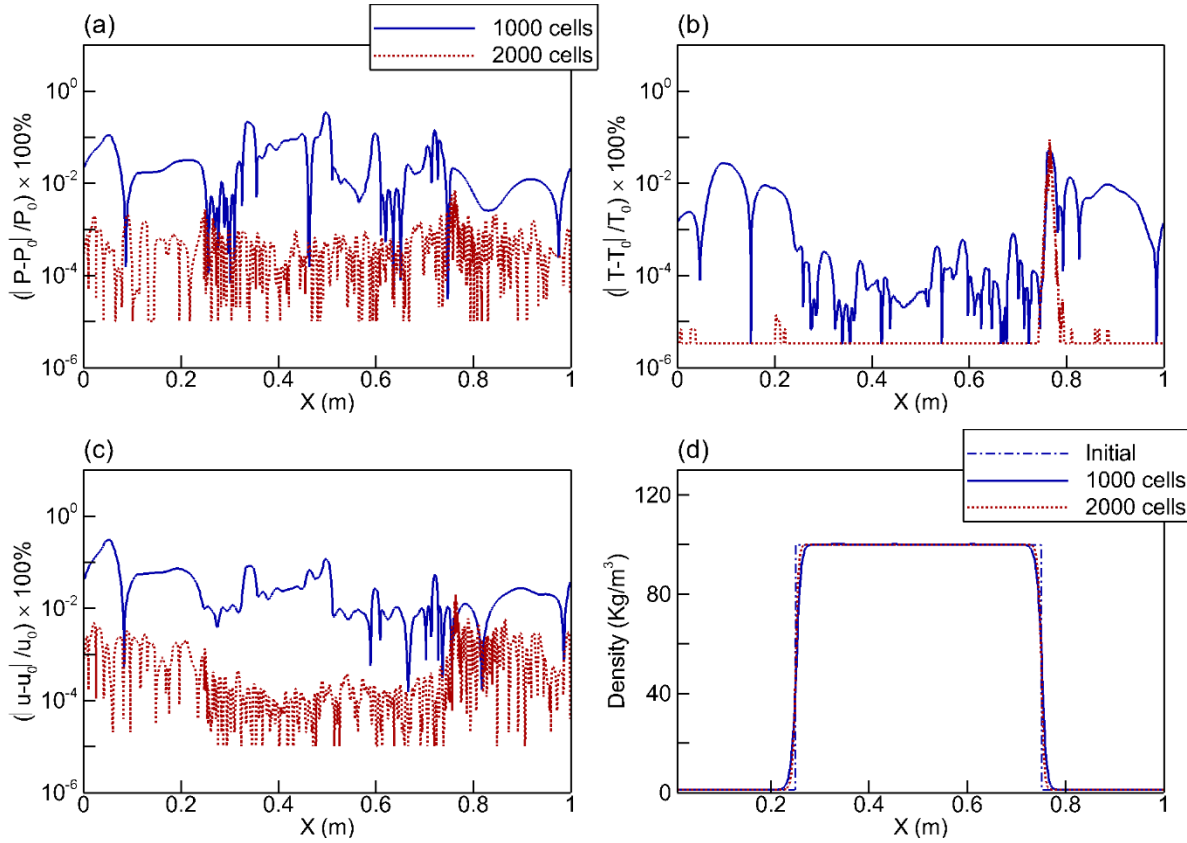
21

Fig. 8 Results of an isolated interface advection tube filled with n-dodecane/nitrogen mixture at 10 ms, errors in (a) pressure, (b) temperature, (c) velocity, and (d) density profile (thin blue dash dot is initial and exact solution, blue solid is 1000 cells, red dashed is 2000 cells, $P = 1$ bar, $T = 300$ K, $Y_{C12H26,l} = 0.99$, $Y_{C12H26,g} = 0.01$, $u = 100$ m/s, CFL = 0.2).

3.3.2 Time-step sensitivity analysis

Another primary numerical parameter is the time-step. The sensitivities of four-equation model to the CFL (Courant–Friedrichs–Lewy) number were investigated, and the results with CFL number in the range of 0.01 – 1.0 for a double-expansion tube (Case 2 in Section 3.1.3) and a shock tube (Case 4 in Section 4.1.1) are plotted in Fig. 9. Numerical instability on the solutions can be observed in the expanding cavitation interface in the case of smallest CFL number, and the instability amplitude is decreased as the CFL number increases. This is because in the present numerical solver, the parabolic terms are solved using the implicit central-differenced method, and hyperbolic is solved explicitly with a second-order upwind approach. Using small CFL number reduces the dissipation of dispersive waves. Therefore, the spurious oscillations increase in time since the dispersion and dissipation errors accumulate as the wave propagates. However, as a large CFL number is used, the numerical diffusion increases across the expansion and shock waves. As expected, the computational time decreases rapidly with raising the CFL number from 0.015 to 0.15. However, as the CFL number subsequently increases, the computational time show insignificant improvement in the computational efficiency. Consequently, based on these numerical results, the best CFL number for four-equation model is in the

22

1 range of 0.15 – 0.3 considering the computational efficiency and stability. In addition, it is noted that

2 the time-step is controlled by the CFL condition when C_{CFL} is small enough. On the contrary, as C_{CFL}

3 is larger than 0.6, the time-step becomes rather controlled by the accuracy conditions.

4
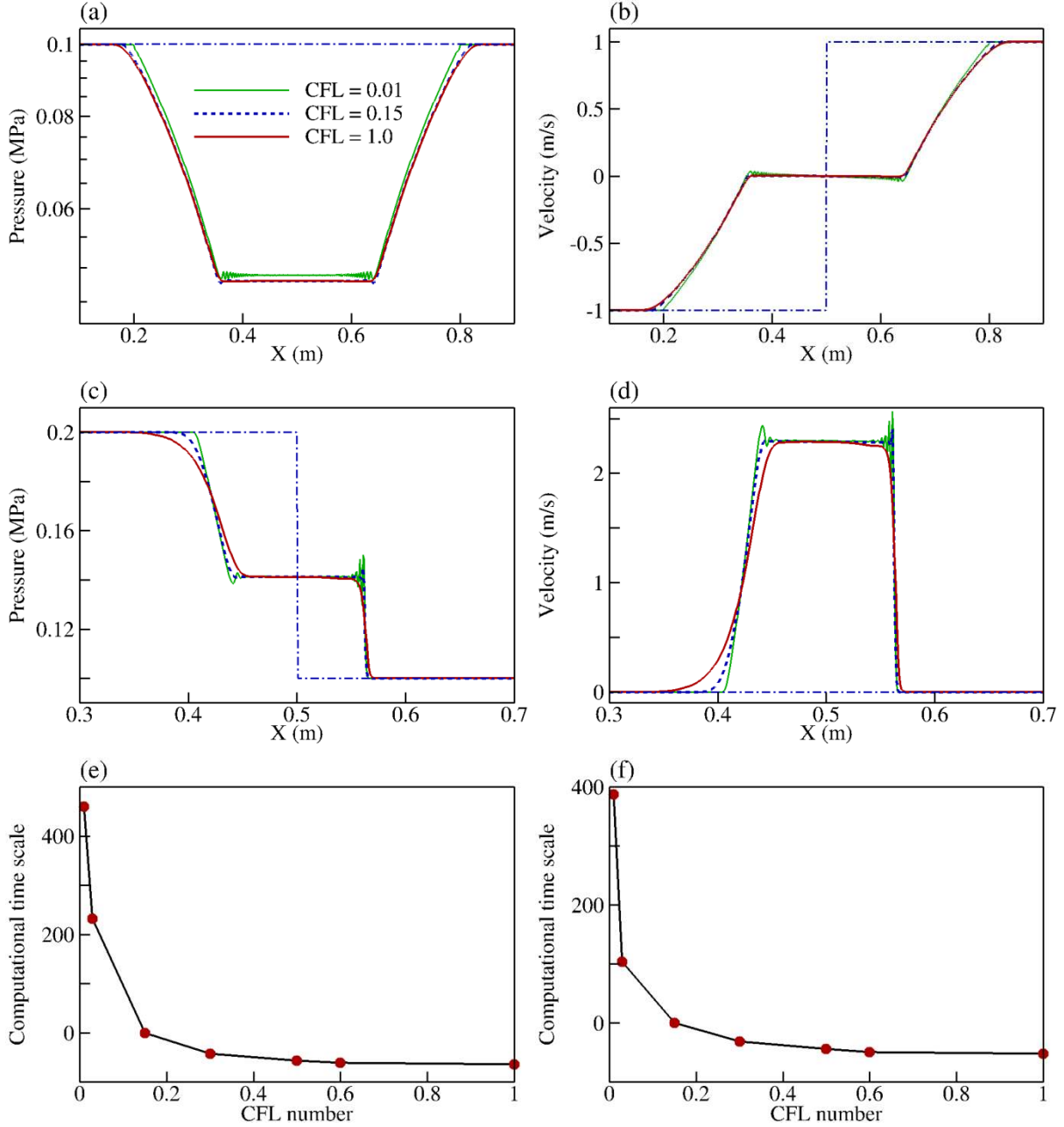
5

6

7

8 Fig. 9 Time-step analysis (CFL number) for Case 2 (*a, b, e, t* = 3.5 ms) and Case 4 (*c, d, f, t* = 2.0 ms),

9 $\varepsilon_{UVn} = 1.0\text{e-}13$, computational time scale $= 100 \times (t_{CFL} - t_{CFL=0.15})/t_{CFL=0.15}$

10

11 3.3.3 Convergence sensitivity analysis

12 To examine the behaviors of UVn flash solver, a convergence analysis was performed. The

13 convergence tolerance is termed as ε_{UVn}. All the objective functions involved in the UVn flash follow

14 the same tolerance. The convergence tolerance is defined as following:

$$\left| \frac{\psi_g - \psi_{g,cal}}{\psi_g} \right| \le \varepsilon_{UVn} \tag{20}$$

$$\left(\ln \left(\frac{f_{k,l}}{f_{k,g}} \right) \right)^2 \le \varepsilon_{UVn} \tag{21}$$

$$\left(\frac{e^* - e_{cal}}{e^*} \right)^2 + \left(\frac{\rho^* - \rho_{cal}}{\rho^*} \right)^2 \le \varepsilon_{UVn} \tag{22}$$

where the subscript *cal* indicates the calculated values during each iteration. The details of each parameter and objective functions in the UVn flash are introduced in Appendix A.3.
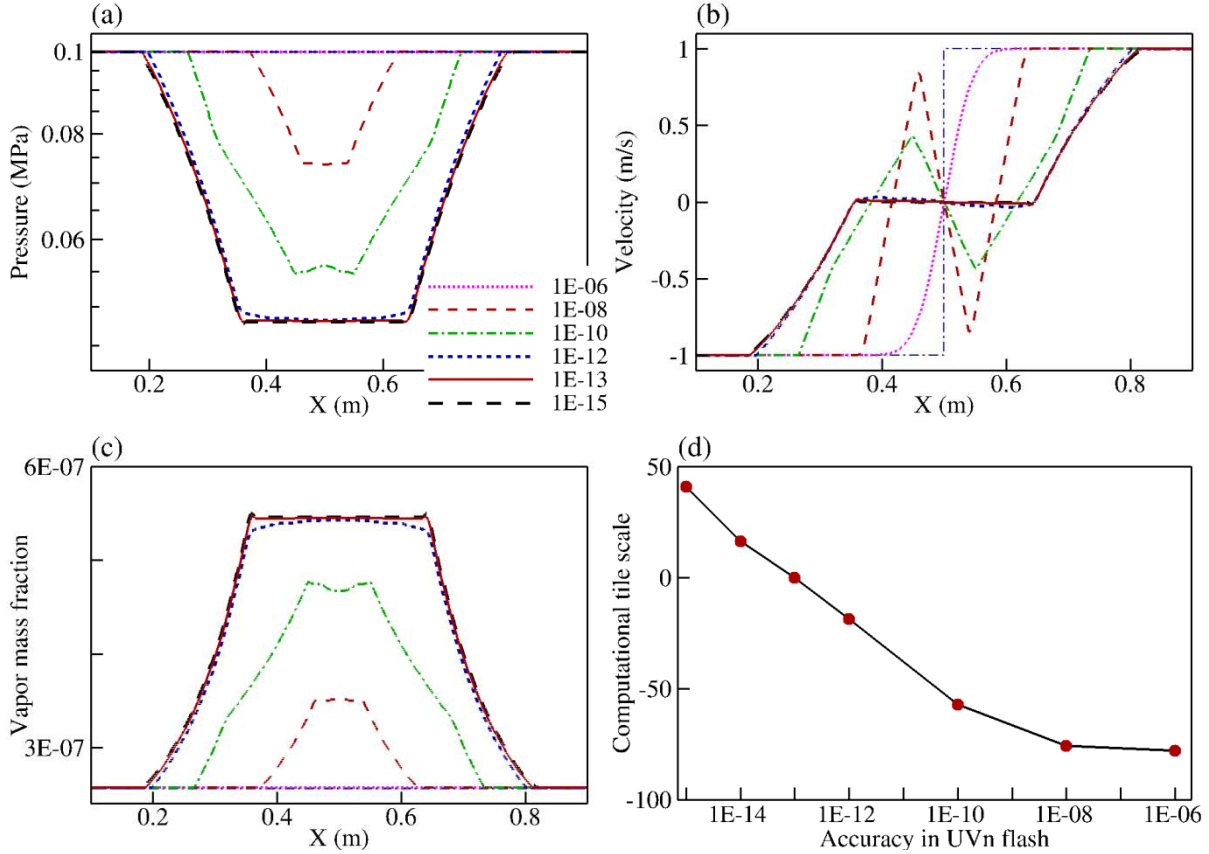

Fig. 10 Convergence analysis of the UVn flash solver (Case 2, $t = 3.5$ ms), computational time scale = $100 \times (t_\varepsilon - t_{\varepsilon=13})/t_{\varepsilon=13}$, thin dash dot lines are initials, CFL = 0.15.

The double-expansion tube (Case 2 in Section 3.1.3) is simulated using the convergence tolerance (ε_{UVn}) in the range of 1.0e-6 – 1.0e-15, and the results are presented in Fig. 10. It is found that there is no phase change during the expansion process with a large convergence tolerance of 1.0e-6. Both the expansion width and phase change quantity rise as the convergence tolerance decreases to the value of 1.0e-13. Moreover, substantial oscillations can be observed in the velocity profile with large convergence tolerance. Notably, the wave of pressure, velocity, as well as the phase change quantity are identical with the strict convergence tolerance of 1.0e-13 – 1.0e-15. Besides, the stricter convergence tolerance leads to longer computational time as expected and shown in Fig. 10(d).

24

1 Considering the compromise between the computational accuracy and efficiency, a convergence

2 tolerance of 1.0e-13 is chosen to get acceptable predictions in the cavitation tube.

3

4 4. Discussion

5 In order to gain better understanding of the complex wave behaviors of *n*-dodecane/nitrogen mixture,

6 especially for the phase change between multicomponent liquid and gas phases, additional five cases

7 are computed, and the details are listed in Table 3 and Table 4.

8

9 4.1 Behaviors of *n*-dodecane/nitrogen mixture in shock tubes

10 In this sub-section, the non-ideal behaviors of *n*-dodecane/nitrogen mixture in shock tubes are

11 discussed based on the numerical results. The tube is filled with high-pressure liquid in the left side

12 and low-pressure gas in the right side. The initial temperature throughout the tube is 293 K on both

13 sides. Two shock tube cases are simulated, one considers tiny discontinuities at the interface between

14 two sides (Case 4), and another case involves large discontinuities in feed (Case 5), as listed in Table 3.

15

16 Table 3. Initial conditions for shock tube cases with *n*-dodecane/nitrogen mixture

	P_L (MPa)	P_R (MPa)	$T_L = T_R$ (K)	$u_L = u_R$ (m/s)	$\alpha_{g,L}$ Equilib.	$\alpha_{g,R}$ Equilib.	$Y_{C_{12},L}$ Input	$Y_{C_{12},R}$ Input
Case 4	0.2	0.1	293	0	0.0117	0.1354	0.9995	0.9995
Case 5	10	0.1	293	0	0.0001	0.9999	0.9788013	0.0211987

17

18 4.1.1 Results of Case 4

19 In Case 4, a mixture with a large amount of *n*-dodecane ($Y_{C_{12}H_{26}} = 0.9995$) is selected as the feed.

20 Since the pressures in left and right sides are different, the initial gas volume fraction at equilibrium

21 state predicted by the TPn flash in left and right sides equals 0.0117 and 0.1354, respectively, which is

22 far from the phase boundaries. Fig. 11 shows the wave evolution behaviors of *n*-dodecane/nitrogen

23 mixture in the shock tube at *t* = 2.0 ms. The conventional expansion and compression waves are

24 shown in Fig. 11(a), and the velocity magnitude depicted in Fig. 11(c) is low due to the high mixture

25 density and tiny gradients in thermodynamic properties. In addition, the large amount of liquid in Case

26 4 shows higher specific heat capacity, thereby the fluid is close to quasi-isothermal even though there

27 is a slight evaporation and condensation. This shock tube case highlights the accuracy of this four-

28 equation model when dealing with tiny gradients in thermodynamic properties.
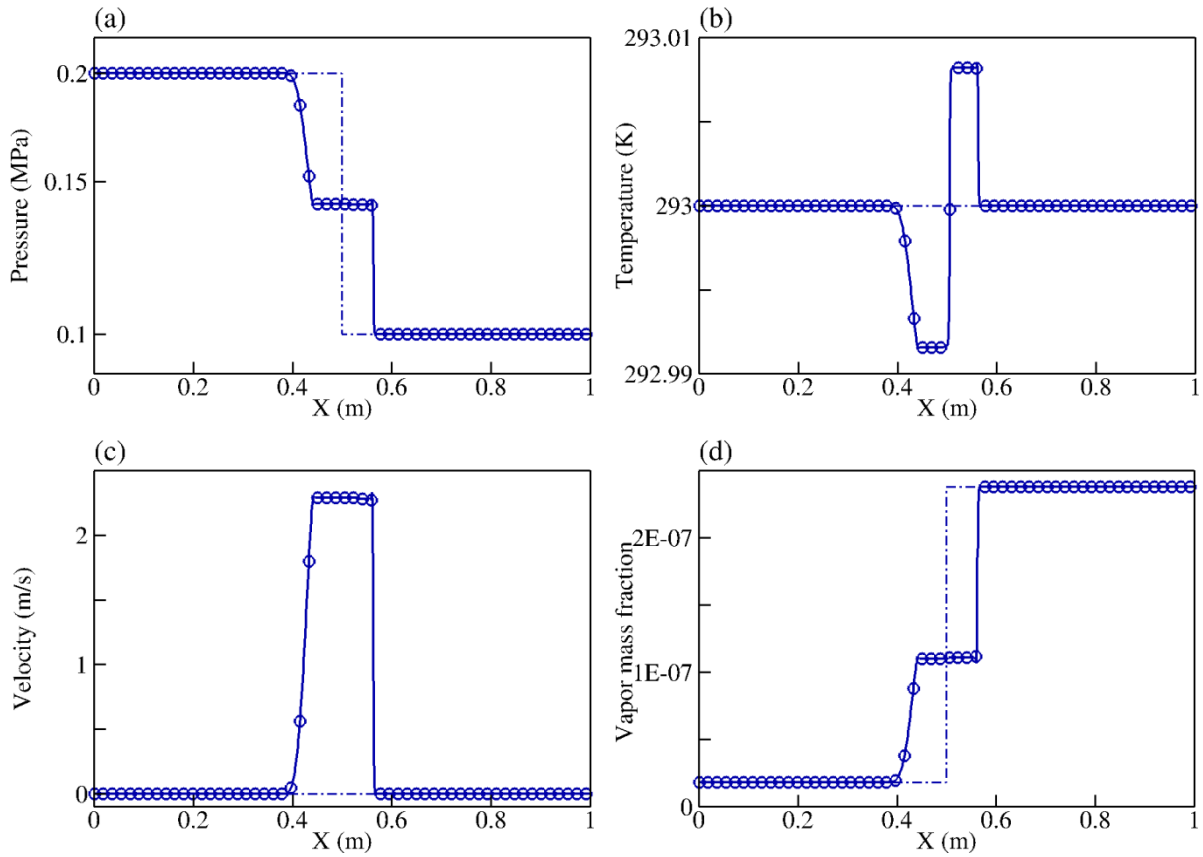
29

Fig. 11 Wave behaviors of *n*-dodecane/nitrogen mixture in the shock tube predicted by the four-equation model (Case 4: $P_L = 0.2$ MPa, $P_R = 0.1$ MPa, $T_L = T_R = 293$ K, $\alpha_{g,L} = 0.0117$, $\alpha_{g,R} = 0.1354$, $t = 2.0$ ms, thin dash dot lines are initials).
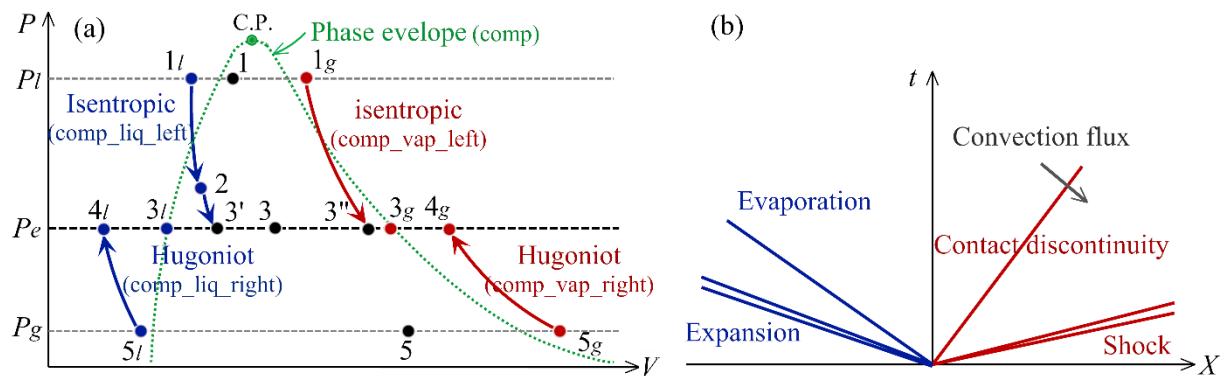
4.1.2 Results of Case 5

Fig. 12 Phase trajectories and wave patterns for fluids (a) phase trajectories; (b) wave patterns (z: mixture composition; y_k_left: gas composition at left; y_k_right: gas composition at right; x_k_left: liquid composition at left; x_k_right: liquid composition at right).

In this case, the input mass fraction of *n*-dodecane in left and right sides of the shock tube diaphragm is 0.9788013 and 0.0211987, respectively. Through the TPn flash, the initial equilibrium α_g in left and right sides is determined as 0.0001 and 0.9999, respectively. The wave evolution profiles of this mixture at the instant of 1.0 ms are plotted in Fig. 13. As the discontinuities of feed at the interface are increased relatively to those in Case 4, the wave behaviors of *n*-dodecane/nitrogen mixture in the shock tube shown in Fig. 13 are more complex than those in Case 4 (Fig. 11). It can be seen that the current model can capture the essential features of the mixture with large gradients in thermodynamic properties. Specifically, four waves can be observed: the left expansion wave, evaporation front, contact discontinuity, and the right shock wave. The detailed wave patterns and phase trajectories are presented in Fig. 12.

Following the analysis of (Saurel et al., 2008), the mixture Hugoniot curve is tagnent to their isentrope, and the multiphase shock waves behave like simple compression waves. Therefore, the phase trajectory of this case with large discontinuities of density can follow the phase schematic of Fig. 12(a). In the left high-pressure side, the initial equilibrium mixture represented by point 1 is composed of large amount of liquid (point 1_l) and a bit gas (point 1_g). As time begins, an expansion wave is generated and travels to the left side with the velocity of $u - C_{s,mix}$, the pressure falls rapidly across the expansion wave. The mass fraction of dissolved nitrogen follows similar evolution behaviors with the pressure as shown in Fig. 13(a) and (b). As known that the dissolved nitrogen is a kind of dense-phase fluid with high vapor pressure, which dramatically enhances the phase change and expansion intensity (Kuijpers et al., 2002). Therefore, it cannot be neglected in the simulation. The initial liquid indicated by point 1_l is expanded to the metastable liquid (point 2) following an isentropic path. In the present modelling, this metastable liquid is relaxed to a thermodynamic equilibrium mixture (point $3'$) through the UVn flash. Thus, the evaporation front appears and travels together with the expansion wave to the left high-pressure side. Both *n*-dodecane vapor and nitrogen gas are produced as shown in Fig. 13(e). The initial gas of point 1_g is expanded following an isentropic path to the point $3''$, which is relaxed to the thermodynamic equilibrium mixture (points 3_g and 3_l) infinitely. The corresponding densities of the mixtures represented by points 1 and 3 ($3 = 3' + 3''$) are reported in Fig. 13(f).
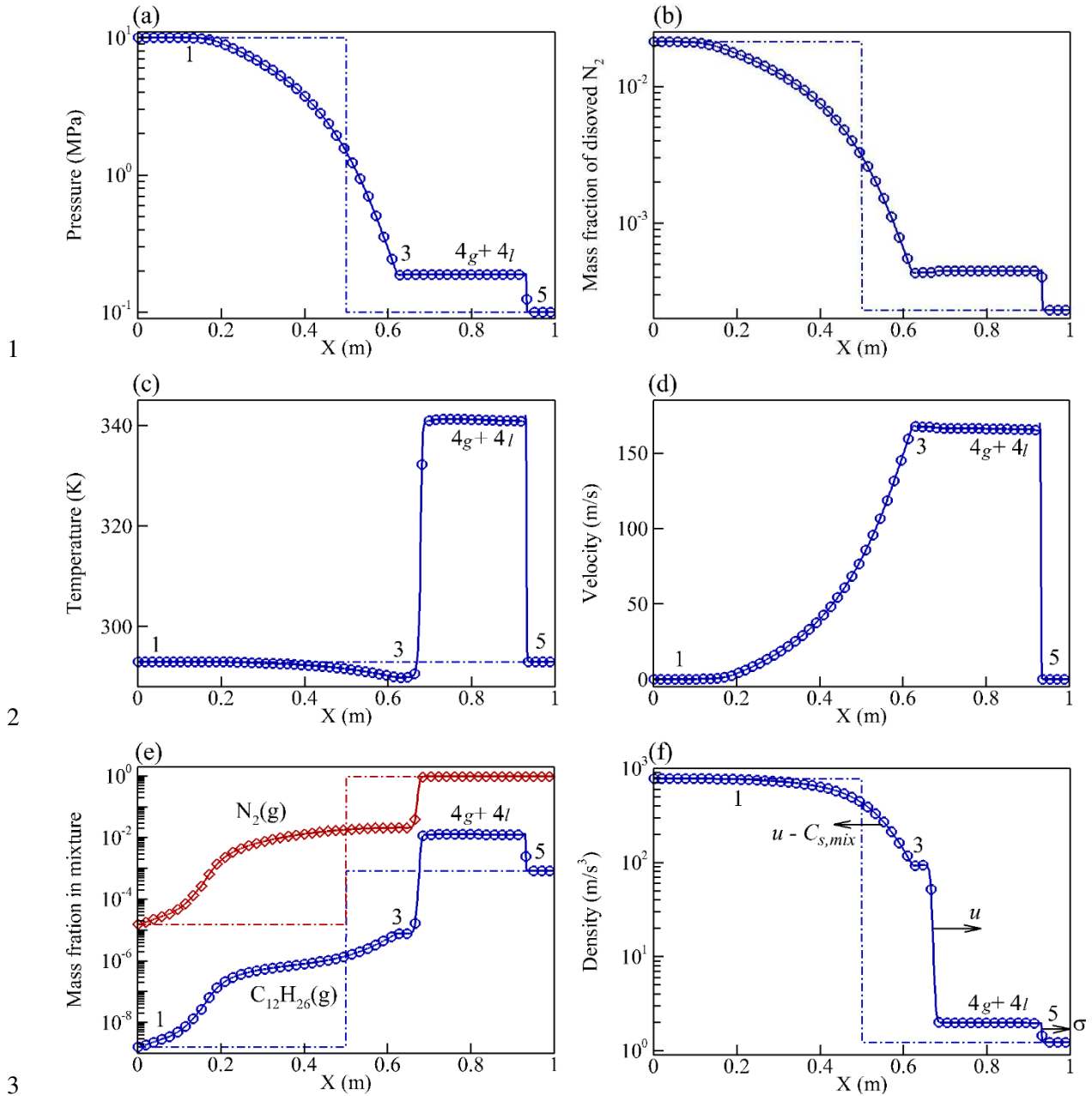
Fig. 13 Wave behaviors of *n*-dodecane/nitrogen mixture in the shock tube predicted by the four-equation model (Case 5: $P_L = 10.0$ MPa, $P_R = 0.1$ MPa, $T_L = T_R = 293$ K, $\alpha_{g,L} = 0.0001$, $\alpha_{g,R} = 0.9999$, $t = 1.0$ ms, thin dash dot lines are initials)

Since there are large discontinuities in densities and species at the contact interface, the liquid at interface undergoes a sudden large phase change in a narrow region (Simões-Moreira, 2000), and the vapor is ejected from the interface and propagated to the right low-pressure side though the convection flux at the velocity of u (Fig. 12(b) and Fig. 13(f)), resulting in an increase in vapor mass fraction (Fig. 13(e)). In the right low-pressure side, the equilibrium mixture of point 5 is composed of large amount of gas (5_g) and small amount of liquid (5_l). At beginning, the shock wave is yielded and propagates to the right low-pressure side at the velocity of σ. The gaseous mixture (5_g) is shocked following a

Hugoniot curve (Saurel et al., 2008) from point 5_g to 4_g as shown in Fig. 12(a). Thus, the pressure, temperature, velocity and the mixture density are increased. Since points 3 and 4_g, as well as 4_l have no thermodynamic connections (Fig. 12(a)), they are only linked by the mechanical equilibrium through a simple contact discontinuity separating the evaporated vapor front and shocked mixtures. Thereby, the pressure and velocity are continuous, while, a sharp contact discontinuity is generated in the profiles of temperature, vapor mass fraction, and density between the mixtures of points 3 and $4_g + 4_l$. The slopes of left expansion and right shock waves can be expressed as $-\rho C_{s,mix}$ and $\rho(\sigma - u)$, respectively. It is noted that the left slop is much lower than the right one (Fig. 13(c)). This is because the sound speed in two-phase mixtures ($C_{s,mix}$) decreases progressively along the expansion evaporation front, following the Wood formula (Wood, 1930). Finally, since the mixture is proven to be in two-phase state during the whole process, no wave splitting has been obtained in the expansion wave.

4.2 Behaviors of *n*-dodecane/nitrogen mixture in double-expansion tubes

In this subsection, three double-expansion tube cases are simulated, and the details are listed in Table 4. In Section 4.2.1, the influence of volume translation in PR-EoS on liquid density is presented. Then, its influence on the expansion behaviors of *n*-dodecane/nitrogen mixture is discussed in the following Sections 4.2.2 – 4.2.4, in which the expansion characteristics under various conditions are included.

Table 4. Initial conditions for double-expansion tube cases with *n*-dodecane/nitrogen mixture

|	$p_L = p_R$ (MPa)	$T_L = T_R$ (K)	u_L (m/s)	u_R (m/s)	$\alpha_{g,L} = \alpha_{g,R}$ Equilib.	$Y_{c12,L} = Y_{c12,R}$ Input
Case 6	0.1	293	-1	1	1.0e-04	0.9997697
Case 7	0.1	480	-1	1	1.0e-04	0.9999349
Case 8	5.0	293	-1	1	1.0e-04	0.9889499

4.2.1 Influence of volume translation in PR-EoS on density and sound speed

The liquid density makes substantial influence on the prediction accuracy for expansion behaviors of the *n*-dodecane/nitrogen mixtures. Since the liquid density of hydrocarbons computed by the PR EoS is known to be inaccurate, the volume translation (Baled et al., 2012, Tapriyal et al., 2012) is added to the PR EoS to improve the prediction accuracy of liquid density as explained in Section 2.1. Results with and without the volume translation for liquid *n*-dodecane density under various temperature and pressure conditions are compared in Fig. 14(a). The test temperature and pressure are in the range of 293 – 480 K and 0.1 – 5.0 MPa, respectively. It can be seen that the model without volume translation substantially underestimates the liquid density compared to NIST data (Linstrom and Mallard, 2001). Comparatively, the predictions with volume translation are improved significantly.

1   Since the dissolved nitrogen quantity in liquid phase is increased with pressure, the effects of

2   dissolved nitrogen on the liquid thermal properties under different pressure conditions need to be

3   illustrated. The compared density and sound speed between the predictions and NIST data at pure

4   liquid sate (TPD = 1 and α_g = 1.0e-06) are illustrated in Fig. 15. The mass fraction of dissolved

5   nitrogen in liquid phase varies from 1.0e-6 to 1.0e-4. It is found that the liquid density and sound

6   speed are insensitive to the dissolved nitrogen quantity at 0.1 MPa condition. However, at the high

7   pressure of 5.0 MPa, both of liquid density and sound speed decrease as the dissolved nitrogen

8   increases. Thereby, it can be concluded that the dissolved nitrogen quantity in the liquid phase is

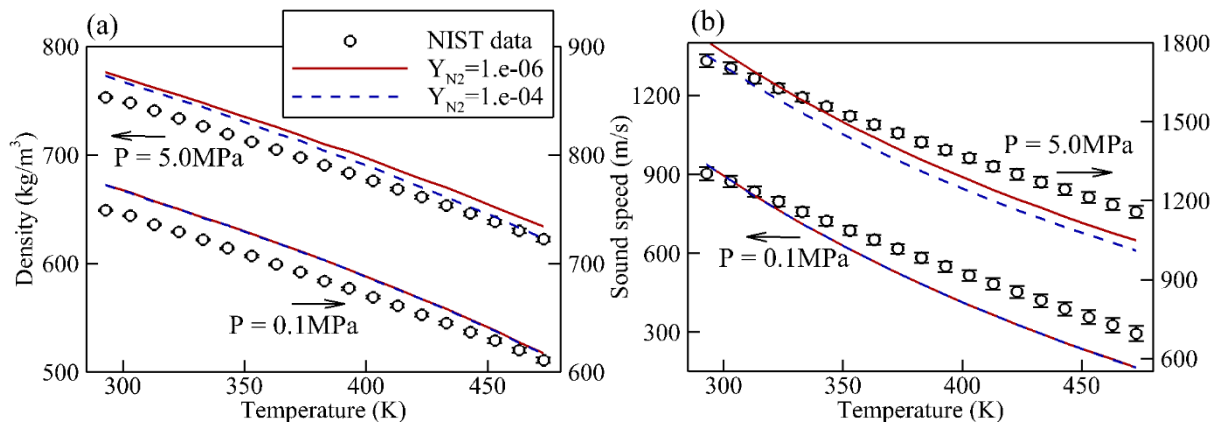9   important for the simulation accuracy at high pressure conditions.

10
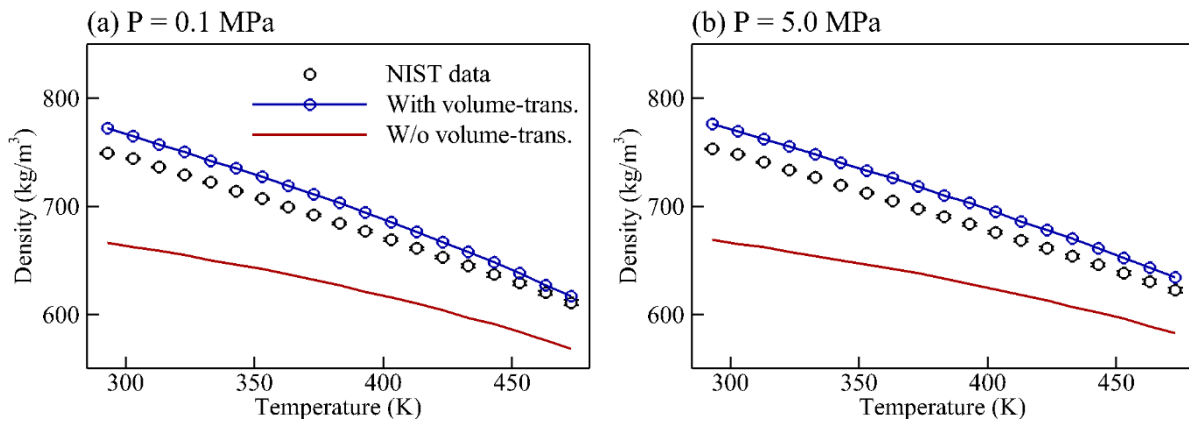
12   Fig. 14 Liquid density of *n*-dodecane predicted by PR-EoS with and without volume translation (circle:

13   data from NIST (Linstrom and Mallard, 2001), α_g = 1.0e-06, Y_{N_2} = 1.0e-04)

14

16   Fig. 15 Effects of the dissolved nitrogen in liquid phase on density and sound speed (circle: data from

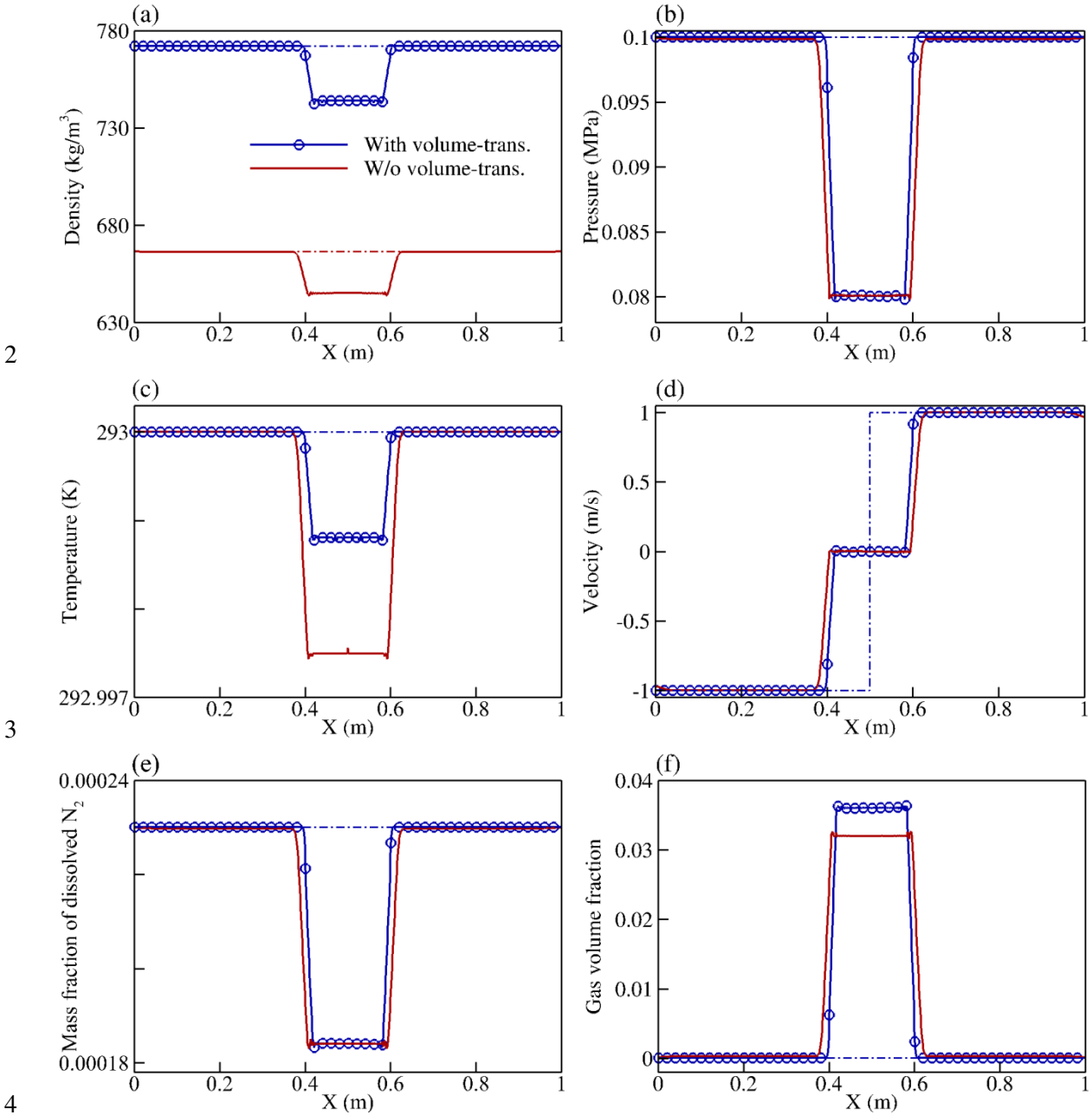17   NIST (Linstrom and Mallard, 2001) for pure liquid *n*-dodecane, α_g = 1.0e-06)

18

19

20

21

4.2.2 Results of Case 6

Fig. 16 Wave behaviors of n-dodecane/nitrogen mixture in the double-expansion tube predicted by the four-equation model with and without volume translation (Case 6: $P_L = P_R = 0.1$ MPa, $T_L = T_R = 293$ K, $\alpha_{g,L} = \alpha_{g,R} = 0.0001$, $u_L = -1.0$ m/s, $u_R = 1.0$ m/s, $t = 3.5$ ms, thin dash dot lines are initials)

The wave patterns of density, speed of sound, pressure, temperature, dissolved nitrogen, as well as the gas phase volume fraction in the double-expansion tube with initial pressure and temperature of 0.1 MPa and 293 K are presented in Fig. 16. The initial velocity of fluid in the left and right sides are -1 and +1 m/s, respectively. As expected, a large discrepancy is shown in the initial density. Ignoring the volume translation underestimates the liquid density about 13%, resulting in a higher expansion rate,

1   and the expanded strength is slightly larger than that predicted by the model with volume translation.

2   A little cooling effect caused by the phase change is captured in the temperature profile. Discrepancies

3   are observed in the evolution of temperature and gas volume fraction predicted by the models with and

4   without the volume translation as shown in Fig. 16(d) and (f). This is due to the heat balance between

5   two phases, the temperature drop and gas volume fraction are estimated by $\Delta T = \left(\rho_g L_{evap} \right) / \left(\rho_l C_{p,l} \right)$

6   and $\alpha_g = 1 / \left[\left(\rho_g L_{evap} / \Delta T \rho_l C_{p,l} \right) + 1 \right]$ (Michel and Franc, 2004). It is found that the liquid density

7   predicted by the model with volume translation is higher than that without volume translation,

8   resulting in a decrease in the temperature drop and an increase in the gas volume fraction.

9

10   4.2.3 Results of Case 7

11   The primary aim of Case 7 is to investigate the influence of temperature on the expansion behaviors

12   for the *n*-dodecane/nitrogen mixture. Fig. 17 presents the profiles of density, pressure, temperature,

13   velocity, dissolved nitrogen, and gas phase volume fraction at 3.5 ms, the initial pressure and

14   temperature of the fluid in the double-expansion tube are 0.1 MPa and 480 K, which is quite close to

15   the boiling temperature of pure *n*-dodecane. Compared to the results of Case 6 with low initial

16   temperature (293 K in Fig. 16), several conclusions can be obtained. First, the liquid density decreases

17   with the temperature increasing. Second, the expanded width is substantially reduced, whereas the

18   cooling effect by the phase change is enhanced by the high temperature. Third, the solubility of

19   nitrogen in liquid phase decreases with an increase in temperature as expected. The mass fraction of

20   nitrogen dissolved in the liquid phase in Case 7 varies from 3.0e-05 to 6.5e-05 (Fig. 17(e)), which is

21   10 times lower than that in Case 6 with low initial temperature (Fig. 16(e)). In addition, since the

22   liquid vapor pressure increases with temperature, the gas content in the cavitation region is increased

23   as shown in Fig. 17(f).

24

25   Based on the results of Fig. 17 for Case 7, the density deviation predicted by the model without

26   volume translation is around 7.5%, which is less than that under the conditions with low initial

27   temperature (around 13% in Case 6). Besides, the evolution of pressure, temperature and velocity

28   predicted by the models with and without volume translation are quite close. Thereby, it can be

29   concluded that the volume translation method shows insignificant effects on the expansion behaviors

30   in Case 7. In other words, it demonstrates that the expansion characteristics of *n*-dodecane/nitrogen

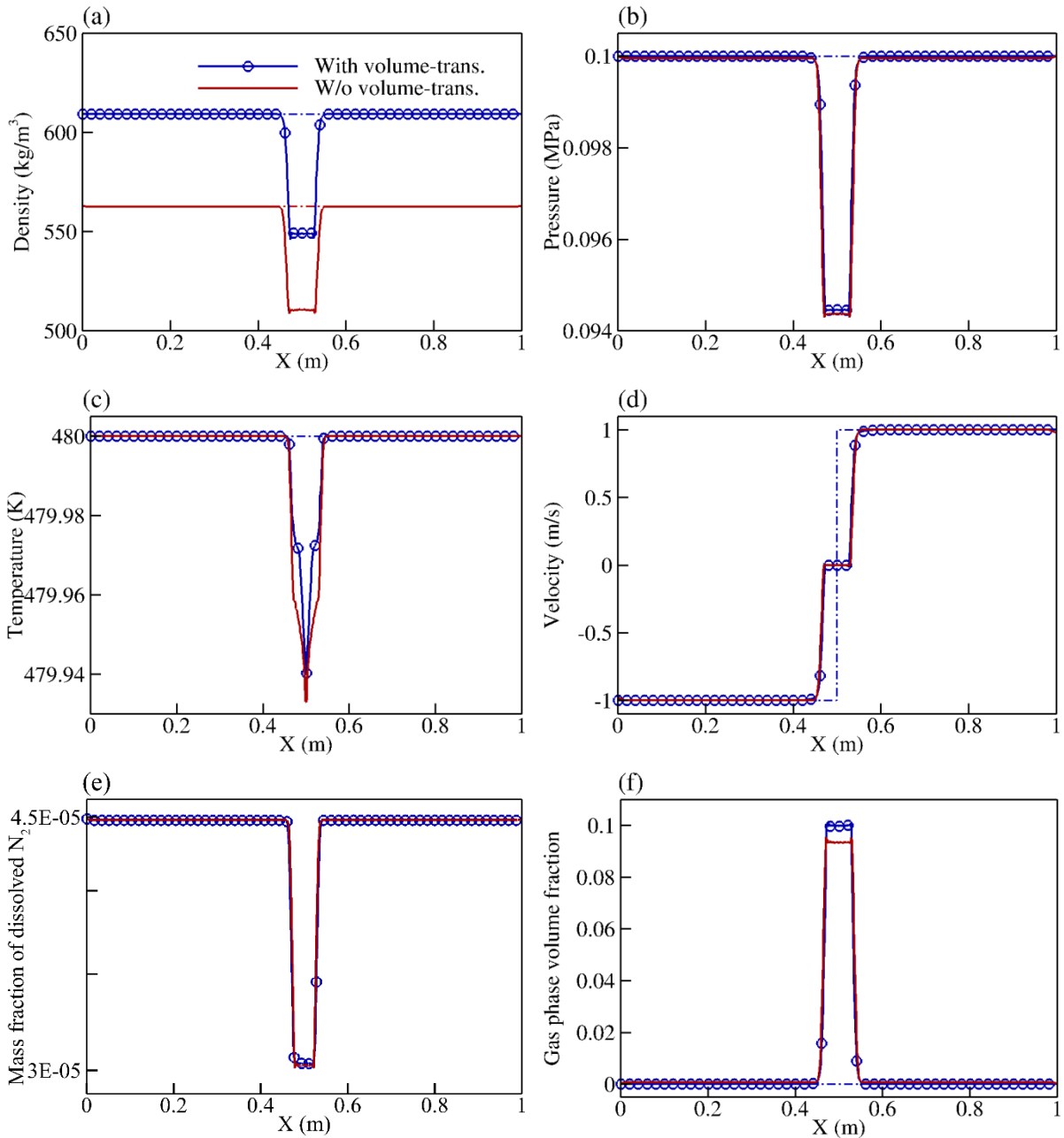31   mixture is non-sensitive to the liquid density at high temperature conditions.

32

Fig. 17 Wave behaviors of *n*-dodecane/nitrogen mixture in the double-expansion tube predicted by the four-equation model with and without volume translation (Case 7: $P_L = P_R = 0.1$ MPa, $T_L = T_R = 480$ K, $\alpha_{g,L} = \alpha_{g,R} = 0.0001$, $u_L = -1.0$ m/s, $u_R = 1.0$ m/s, $t = 3.5$ ms, thin dash dot lines are initials)

4.2.4 Results of Case 8

Another important variable for expansion behaviors is pressure. The wave evolution profiles of *n*-dodecane/nitrogen mixture in the double-expansion tube are presented in Fig. 18. The initial temperature and pressure of fluid are 293 K and 5.0 MPa. Compared to the results of Case 6 with low initial pressure (0.1 MPa), the expanded speed and the dissolved nitrogen quantity are increased remarkably in Case 8 with high initial pressure (5.0 MPa). The mass fraction of dissolved nitrogen in

the liquid phase is seen to be as large as 0.01105 (see Fig. 18(e)), since the dissolved nitrogen possess a high vapor pressure, it can improve the phase change and expansion intensity a lot (Kuijpers et al., 2002). Thereby, it can be concluded that the multicomponent two-phase flow model, such as this four-equation model, is strongly required for accurately predicting the homogeneous nucleation during the pressure expansion processes, like in diesel and GDI engines with high injection pressures.
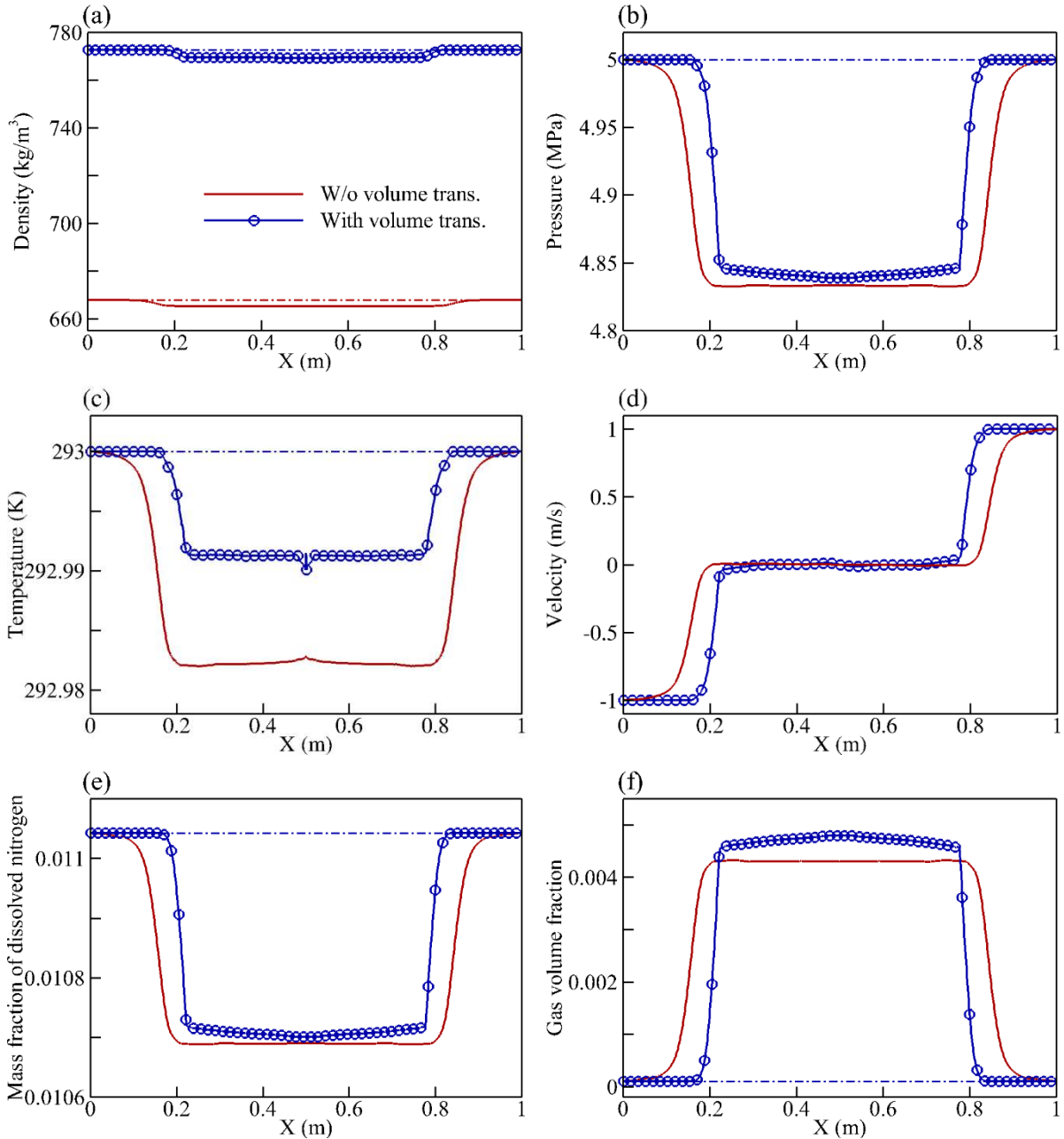
Fig. 18 Wave behaviors of *n*-dodecane/nitrogen mixture in the double-expansion tube predicted by the four-equation model with and without volume translation (Case 8: $P_L = P_R = 5.0$ MPa, $T_L = T_R = 293$ K, $\alpha_{g,L} = \alpha_{g,R} = 0.0001$, $u_L = -1.0$ m/s, $u_R = 1.0$ m/s, $t = 1.4$ ms, thin dash dot lines are initials).

As the pressure increases, the volume translation added in PR EoS becomes very important in density predictions and subsequently influences the expansion behaviors. The compared results between the models with and without volume translation are plotted in Fig. 18. Large deviation can be observed in the expansion width predicted by the model without volume translation. Therefore, the volume translation is demonstrated to be important in the real-fluid simulation using PR EoS, especially at high pressure conditions.

5. Three-dimensional n-dodecane injection modelling

To study the performance of the proposed four-equation model for multidimensional flows, a 3D transcritical fuel injection is simulated. Here, the transcritical injection is defined as that both injection and chamber pressures exceed the fluid critical pressure, and the injection temperature is lower but the chamber temperature is higher than the fluid critical temperature (Ma et al., 2017). Therefore, the injected fluid follows a path crossing the pseudo-boiling line and evolves from a liquid-like state to a gas-like state at T_{pseudo} as reported recently by (Banuti, 2015) and (Yang et al., 2018). In this simulation, the phase change is not expected. The computational domain is illustrated in Fig. 19(a). A typical injector which consists of a single-hole (Length = 1 mm and Diameter = 100 µm) is fitted to a hexahedral chamber. The boundary conditions are set with pressure inlet and outlet in left and right sides of the geometry, respectively, as shown in Fig. 19(b). A liquid n-dodecane (index C_{12}) jet at 363 K ($T_{jet} < T_{c,C_{12}} = 658.1$ K) is injected into a chamber filled with vapor n-dodecane at the temperature of 900 K ($T_{chamber} > T_{c,C_{12}}$). The injector and chamber pressures are initially set to be 7 and 4 MPa, respectively, which are above the n-dodecane critical pressure ($P_{c,C_{12}} = 1.82$ MPa).

Fig. 19 Schematic and mesh distribution of a typical injector (a) Schematic; (b) Mesh (204800 cells, the minimum size is 10 µm).

The density, temperature, and isobaric heat capacity behaviors at the instant of 0.09 ms are plotted in Fig. 20(a). The jet is evolving from a liquid-like supercritical state ($T < T_{pseudo}$) to a gas-like supercritical state ($T > T_{pseudo}$). The fluid thermodynamic state is correctly predicted as shown in Fig. 20(b). Indeed, the predicted density and isobaric heat capacity agree very well with the available NIST data (Linstrom and Mallard, 2001). In particular, the non-linearity of isobaric across the pseudo-boiling line seems to be well captured by the PR EoS. This phenomenon appears at the jet periphery and also in the jet front (see C_p in Fig. 20(a). The peak value of isobaric heat capacity is very large (around 4 kJ/(kg·K)), which may have significant cooling effects on the temperature distribution

before combustion. Of course, this kind of non-linearity behavior cannot be obtained by the ideal gas EoS (Segal and Polikhov, 2008). Therefore, to better quantify the performance of transcritical injection and combustion, the real-fluid two-phase flow model should be considered.
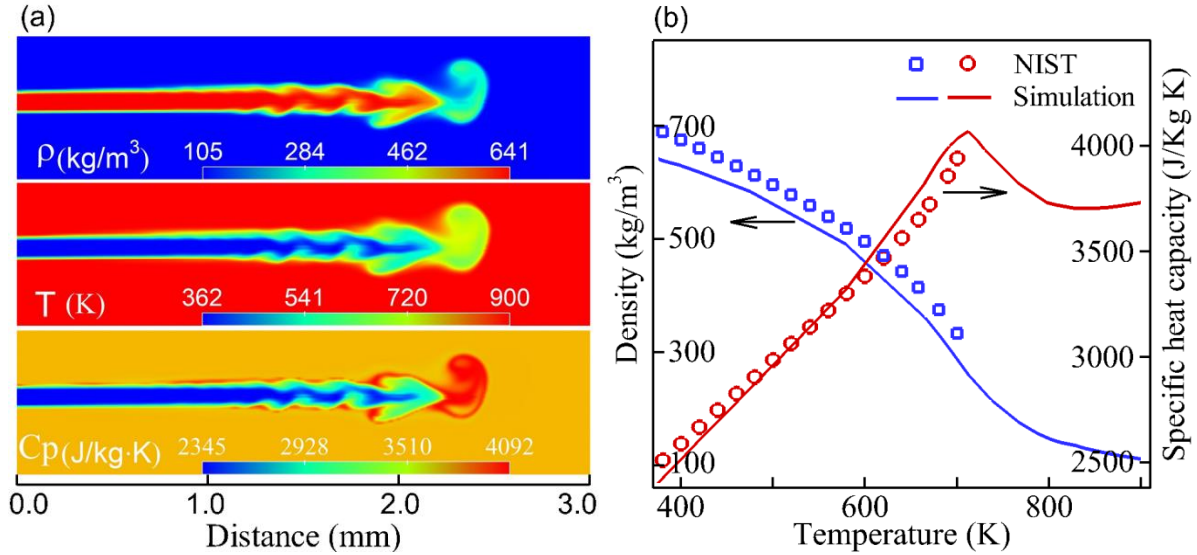
Fig. 20 Results of injection event (a) temporal sequence of density (ρ), temperature (T), and isobaric heat capacity (C_p); (b) comparison between predicted density and isobaric heat capacity with available NIST data (Here, the density and heat capacity varied with temperature are in the radial section at the distance of 1.85 mm from the hole exit), ($P_{jet} = 7.0$ MPa, $T_{jet} = 363$ K, $P_{chamber} = 4.0$ MPa, $T_{chamber} = 900$ K, $Y_{c12h26} = 0.99999$, $t = 0.09$ ms).

6. Conclusions

A multicomponent fully compressible four-equation model with a real-fluid equilibrium-solver was constructed and implemented into an in-house IFP-C3D software. It was validated against the experimental results, and the capability to deal with two-phase flows was highlighted in both 1D and 3D test cases. According to the numerical results, the following conclusions can be obtained.

(1) The suggested four-equation model can compute the real-fluid phase change for multicomponent two-phase flows, and it can also predict more accurate real-fluid behaviors, including the effects of dissolved nitrogen in liquid phase;

(2) The "composite EoS" approach using respective PR EoS in their range of convexity for liquid and gas phases, and connected in the vapor dome by a set of equilibrium constraints, can solve the drawback of "mixture PR EoS" in the unstable spinodal region, and so preserve the hyperbolicity of the Euler system;

(3) Referring to the wave behaviors of water-nitrogen in the 1D shock and double-expansion tubes with tiny discontinuities at the interface, the predictions of present four-equation model are close to those of Chiapolino et al. (2017) model;

(4) The flash boiling process of *n*-dodecane/nitrogen mixture is satisfactorily reproduced by the present four-equation model, and the predicted results show good agreements with experimental measurements. The complex wave patterns in flash boiling cases are successfully tracked;

(5) Based on the sensitivity analysis, this four-equation model can illustrate reliable and efficient calculations with a convergence criterion of 1.0e-13 and a CFL number in the range of 0.15 – 0.3;

(6) This four-equation model can produce the complex wave behaviors satisfactorily, including the expansion, evaporation and shock fronts, as well as the contact discontinuity regime for *n*-dodecane/nitrogen mixtures with large discontinuities at the interface. The wave evolutions have been revealed and analyzed based on the thermodynamic phase trajectories under various conditions;

(7) The dissolved nitrogen quantity in liquid phase becomes larger as the pressure increases and temperature decreases, its evolution profile is quite close to the pressure. The phase change and cavitation intensity are improved with large amount of dissolved nitrogen in the liquid phase;

(8) The volume translation in PR EoS shows negligible effects on the liquid density, expansion behaviors for the *n*-dodecane/nitrogen mixture in the cases with high initial temperature. However, as the initial pressure increases and temperature decreases, the volume translation model may help to obtain the correct density and expansion behaviors.

(9) Finally, the suggested four-equation model has been shown to be able of predicting the main features of a typical 3D subcritical and transcritical injections.

Declarations of interest: none

Appendix A. Thermodynamic properties and equilibrium-solver

A.1. Thermodynamic properties of single-phase

Thermodynamic parameters in this study are evaluated consistently with PR EoS, including the pressure, specific internal energy, density, and the fugacity of species:

$$\left.\frac{\partial P}{\partial T}\right|_\rho = \frac{R}{V-b} - \frac{da}{dT}\frac{1}{V^2+2bV-b^2} \tag{A. 1}$$

$$\left.\frac{\partial P}{\partial \rho}\right|_T = -\frac{M}{\rho^2}\left[\frac{-RT}{(V-b)^2} + \frac{2a(V+b)}{(V^2+2bV-b^2)^2}\right] \tag{A. 2}$$

$$e_d = \left.\frac{\partial e}{\partial T}\right|_P = \left(T\frac{da}{dT} - a\right)\ln\left(\frac{V+(1+\sqrt{2})b}{V+(1-\sqrt{2})b}\right)/(2\sqrt{2}bM) \tag{A. 3}$$

$$e = e_0 + e_d \tag{A. 4}$$

$$\left.\frac{\partial \rho}{\partial T}\right|_P = -\left.\frac{\partial P}{\partial T}\right.\left(\left.\frac{\partial P}{\partial \rho}\right|_T\right)^{-1} \tag{A. 5}$$

$$f_k = x_k\phi_k \tag{A. 6}$$

$$\phi_k = exp\left(\left(\frac{b_k}{B}\right)(Z-1) - \ln(Z-B) + \left(\frac{A}{2\sqrt{2}B}\right)\left[\frac{b_k}{B} - \frac{2.0}{A\alpha}\sum_{k'=1}^{N} x_{k'}a_{k'}\alpha_{kk'}\right]\ln\left(\frac{Z+2.414B}{Z-0.414B}\right)\right) \tag{A. 7}$$

where e is the internal energy, which is computed from the sum of the departure part of e_d (Vidal, 2003) and the ideal gas part e_0, which is calculated based on the polynomial equation (Aly and Lee, 1981). ϕ_k is fugacity coefficient; Z is compressibility factor, calculated as

$$Z^3 - (1-B)Z^2 + (A - 3B^2 - 2B)Z - (AB - B^2 - B^3) = 0 \tag{A. 8}$$

where $A = aP/R^2T^2$ and $B = bP/RT$; the coefficients a and b are estimated based on the van der Waals mixing rule as $a = \sum\sum x_{k_1}x_{k_2}a_{k_1k_2}$, $b = \sum x_{k_1}b_{k_1}$, a_k and b_k are determined based on the critical point of each component (Kwak and Mansoori, 1986), $k_{k_1k_2} = 0.19$ for n-dodecane/nitrogen and $k_{k_1k_2} = 0.0$ for water-nitrogen in this study.

A.2. Phase stability test

The phase stability test is an important part of phase equilibrium computation. It is used to decide whether the system is thermodynamically stable. In this study, the Tangent Plane Distance (TPD) criterion (Michelsen, 1982) is used. In this approach, the TPD represents the vertical distance from the tangent hyperplane of Gibbs free energy surface at the feed z_k to that at the phase compositions x_k. The system stability requires the TPD function to be non-negative:

$$TPD = \sum_k^N x_k\left[\mu_k(x_k) - \mu_{k,0}(z_k)\right] \geq 0 \tag{A. 9}$$

where x_k denotes the mole fraction of component k in one assumed phase. If non-negative TPD value is obtained with any trial phase compositions x_k, the initial mixture is stable and no phase split is needed. Otherwise, the initial mixture with the feed z_k is unstable, then the phase split happens. In this study, the label TPD = N_{phase} is used to identify the nature of phase with $N_{phase} = 0$ for pure gas, $N_{phase} = 1$ for pure liquid and $N_{phase} = 2$ for two-phase.

A.3. Isoenergetic-Isochoric (UVn) flash

Assuming the instantaneous thermodynamic equilibrium in each control volume, an isoenergetic-isochoric (UVn) flash is used to relax the Gibbs free energy of each phase. The mixture specific internal energy and density (e^*, ρ^*) are known from the flow-solver (Eqs. (1) – (4)). The temperature, pressure, equilibrium factor, and vapor fraction (T, P, K_k, ψ_g) are iterated based on the equilibrium solver (Eqs. (11) – (14)). The UVn flash iteration is composed of two parts: (1) Inner loop (TPn flash) and (2) Outer loop.

A.3.1 Inner loop – Isothermal-isobaric (TPn) flash

In the TPn flash (Saha and Carrolls, 1997), the phase compositions (x_k, y_k) are the target variables, but they are not independent, the equilibrium factor (K_k) and vapor fraction (ψ_g) are. The equilibrium factor (K_k) is defined as

$$K_k = y_k/x_k \tag{A. 10}$$

where the phase compositions can be described as

$$y_k = z_k K_k/\left[1 + (K_k - 1)\psi_g\right] \tag{A. 11}$$
$$x_k = z_k/\left[1 + (K_k - 1)\psi_g\right] \tag{A. 12}$$

where $\sum_{k=1}^{N} y_k = \sum_{k=1}^{N} x_k = 1$. The objective functions in TPn flash are Rachford-Rice equation (Saha and Carrolls, 1997) and fugacity equality equation described as

$$F_1 = \sum_{k=1}^{N} z_k(K_k - 1)/\left[1 + \psi_g(K_k - 1)\right] \tag{A. 13}$$
$$F_2 = f_{k,l}/f_{k,g} - 1 \tag{A. 14}$$

First, the objective function of Eq. (A. 13) is iteratively solved to obtain the vapor fraction ψ_g. Then, the second objective function (A. 14) is solved to get the equilibrium constant (K_k). The inner loop is iterated until the convergence tolerance is fulfilled as Eq. (21). Otherwise, Eqs. (A. 13) and (A. 14) are solved again with the new estimates for ψ_g and K_k. After the TPn flash, we can obtain the vapor mass fraction and equilibrium constant (ψ_g and K_k). The phase compositions (x_k, y_k) can be determined based on Eqs. (A. 11) – (A. 12).

The initializations of ψ_g and K_k are given by the solutions of flow-solver at current time-step n, as

$$\psi_{g,n\_UVn^0} = \psi''_{g,n} = m''_{g,n}/\left(M_g \sum n''_{k,g}\right) \tag{A. 15}$$
$$K_{k,n\_UVn^0} = \phi''_{k,l}/\phi''_{k,g} \tag{A. 16}$$

where the subscript (n_UVn^0) represents the initial values of UVn flash, and superscript (") indicates the non-equilibrium values obtained from the flow-solver. Notably, the TPn flash is not only used in the inner loop of UVn flash to compute the phase compositions, but also applied in the initialization to calculate the initial equilibrium phase compositions (x_k, y_k) (see Step (3) in Section 2.3).

A.3.2 Outer loop

In the outer loop, the specific internal energy and density of each phase are calculated by updating the dependent variables of temperature and pressure with the phase compositions obtained from the TPn flash. The objective functions are expressed as:

$$F_3 = \frac{e^* - \sum_{p=1}^{2} \psi_p M_p e_p/\bar{M}}{e^*} \tag{A. 17}$$
$$F_4 = \frac{\rho^* - \bar{M}/\sum_{p=1}^{2} \psi_p M_p/\rho_p}{\rho^*} \tag{A. 18}$$

The outer loop is performed using the initial estimates ($P_{n\_UVn^0}$ and $T_{n\_UVn^0}$) and a Newton iterative algorithm (Saha and Carrolls, 1997). The internal energy and density of each phase (e_p and ρ_p) are computed based on the temperature derivatives of internal energy and density (Eqs. (A. 3) and (A. 5)), as well as the pressure derivatives of density (Eq. (A. 2)). The first-order Taylor series approximation

1   with the relaxation coefficient ($f_{rela} = 1 - \Delta T/T$) is used to estimate the temperature and pressure

2   variations (ΔT and ΔP) as

3
$$\Delta T = \frac{e^* - \sum_{p=1}^{2} \psi_p M_p e_p / \overline{M}}{\partial e / \partial T}, \quad \Delta P = \Delta T \left.\frac{\partial V}{\partial T}\right|_P \left.\frac{\partial P}{\partial V}\right|_T \tag{A. 19}$$

4   Therefore, the current pressure and temperature (P and T) can be updated by $P = P + f_{rela}\Delta P$ and

5    $T = T + f_{rela}\Delta T$, respectively. The calculation of UVn flash is stopped if $(F_3^2 + F_4^2) \leq \varepsilon_{UVn}$.

6   Otherwise, the TPD stability test is applied again to determine the phase stability: if TPD = 2, update

7   the pressure and temperature (P and T) again following Eq. (A. 19), and the TPn flash is iteratively

8   solved again with the new estimates for P and T until $F_1 \leq \varepsilon_{UVn}$ and $F_2 \leq \varepsilon_{UVn}$; if TPD = 0 or 1, the

9   mixture is assumed to be stable, and only the pressure and temperature (P and T) are updated based on

10   Eq. (A. 19) without the TPn flash. In the outer loop of UVn flash, the pressure and temperature (P and

11   T) are initialized by the solutions at equilibrium state obtained from the UVn flash in the previous

12   time-step (denoted $n - 1$) as

13
$$P_{n\_UVn^0} = P_{n-1}, T_{n\_UVn^0} = T_{n-1} \tag{A. 20}$$

14   Note that for $n = 1$, the input initial values P_0 and T_0 are used.

15

16   A.4 Analytical solution of Cubic equation

17   There are three roots when solving the cubic EoS (e.g., PR EoS). In this study, an exact analytical

18   solution of cubic EoS is adopted based on the approach of (Perry, 1950, Wilczek‐Vera and Vera,

19   2015). During the calculation, the non-physical meaning roots like negative or conjugate complex

20   values will appear. However, these non-physical roots are excluded, and only real positive roots are

21   selected. The detailed analytical solution is described as following:

22
$$x^3 + Ax^2 + Bx + C = 0 \tag{A. 21}$$

23   where, A, B and C are numerical coefficients.

24

25   Firstly, two coefficients, D and E, are defined as:

26
$$D = \left(\frac{A}{3}\right)^3 - \left(\frac{AB}{6}\right) + \frac{C}{2} \tag{A. 22}$$

27
$$E = \left(\frac{B}{3}\right) - \left(\frac{A}{3}\right)^2 \tag{A. 23}$$

28

29   Then, the discriminant is computed as $\Delta = D^2 + E^2$.

30

31   (1) If $\Delta = 0$, there are three roots with at least two equal roots as:

32
$$x_1 = 2\sqrt[3]{-D} - \left(\frac{A}{3}\right), \quad x_2 = x_3 = -\sqrt[3]{-D} - \left(\frac{A}{3}\right) \tag{A. 24}$$

33   (2) If $\Delta > 0$, there are one real root and two complex conjugate roots. Two other coefficients F, G are

34   defined as:

1

$$F = \sqrt[3]{(-D) + \sqrt{\Delta}}, \ G = \sqrt[3]{(-D) - \sqrt{\Delta}} \qquad (A.\,25)$$

2   The roots are formulated as:

3

$$\begin{cases} x_1 = F + G - \left(\frac{A}{3}\right) \\ x_2 = -\left[\frac{1}{2}(F+G) + \frac{A}{3}\right] + \frac{\sqrt{3}}{2}(F-G)i \\ x_3 = -\left[\frac{1}{2}(F+G) + \frac{A}{3}\right] - \frac{\sqrt{3}}{2}(F-G)i \end{cases} \qquad (A.\,26)$$

4   (3) If $\Delta < 0$, there are three real and unequal roots. A new parameter θ is defined as:

5

$$\theta(radians) = \arccos\left(\frac{-D}{\sqrt{-E^3}}\right) \qquad (A.\,27)$$

6   The three roots are formulated as:

7

$$\begin{cases} x_1 = 2\sqrt{-E}\cos\left(\frac{\theta}{3}\right) - \frac{A}{3} \\ x_2 = 2\sqrt{-E}\cos\left(\frac{\theta}{3} + \frac{2}{3}\pi\right) - \frac{A}{3} \\ x_3 = 2\sqrt{-E}\cos\left(\frac{\theta}{3} + \frac{4}{3}\pi\right) - \frac{A}{3} \end{cases} \qquad (A.\,28)$$

8

Reference

Allaire, G., S. Clerc, S. Kokh, 2002. A five-equation model for the simulation of interfaces between compressible fluids. Journal of Computational Physics 181, 577-616.

Aly, F.A., L.L. Lee, 1981. Self-consistent equations for calculating the ideal gas heat capacity, enthalpy, and entropy. Fluid Phase Equilibria 6, 169-179.

Amsden, A.A., 1997. KIVA-3V: A block-structured KIVA program for engines with vertical or canted valves. Los Alamos National Lab., NM, United States.

Amsden, A.A., P. O'rourke, T. Butler, KIVA-II: A computer program for chemically reactive flows with sprays. 1989, Los Alamos National Lab., NM (USA).

Andrianov, N., R. Saurel, G. Warnecke, 2003. A simple method for compressible multiphase mixtures and interfaces. International Journal for Numerical Methods in Fluids 41, 109-131.

Baer, M., J. Nunziato, 1986. A two-phase mixture theory for the deflagration-to-detonation transition (DDT) in reactive granular materials. International Journal of Multiphase Flow 12, 861-889.

Baled, H., R.M. Enick, Y. Wu, M.A. McHugh, W. Burgess, D. Tapriyal, B.D. Morreale, 2012. Prediction of hydrocarbon densities at extreme conditions using volume-translated SRK and PR equations of state fit to high temperature, high pressure PVT data. Fluid Phase Equilibria 317, 65-76.

Banuti, D., 2015. Crossing the Widom-line–Supercritical pseudo-boiling. The Journal of Supercritical Fluids 98, 12-16.

Battistoni, M., S. Som, D.E. Longman, 2014. Comparison of mixture and multifluid models for in-nozzle cavitation prediction. Journal of Engineering for Gas Turbines and Power 136, 061506.

Beig, S.A., E. Johnsen, 2015. Maintaining interface equilibrium conditions in compressible multiphase flows using interface capturing. Journal of Computational Physics 302, 548-566.

Bohbot, J., N. Gillet, A. Benkenida, 2009. IFP-C3D: an unstructured parallel solver for reactive compressible gas flow with spray. Oil & Gas Science and Technology-Revue de l'IFP 64, 309-335.

Castier, M., 2009. Solution of the isochoric–isoenergetic flash problem by direct entropy maximization. Fluid Phase Equilibria 276, 7-17.

Chiapolino, A., P. Boivin, R. Saurel, 2017. A simple and fast phase transition relaxation solver for compressible multicomponent two-phase flows. Computers & Fluids 150, 31-45.

Chung, T.H., M. Ajlan, L.L. Lee, K.E. Starling, 1988. Generalized multiparameter correlation for nonpolar and polar fluid transport properties. Industrial & Engineering Chemistry Research 27, 671-679.

Courant, R., K.O. Friedrichs, 1999. Supersonic flow and shock waves. Springer Science & Business Media.

Espósito, R.O., M. Castier, F.W. Tavares, 2000. Calculations of thermodynamic equilibrium in systems subject to gravitational fields. Chemical Engineering Science 55, 3495-3504.

Flåtten, T., H. Lund, 2011. Relaxation two-phase flow models and the subcharacteristic condition. Mathematical Models and Methods in Applied Sciences 21, 2379-2407.

Goncalvès, E., B. Charrière, 2014. Modelling for isothermal cavitation with a four-equation model. International Journal of Multiphase Flow 59, 54-72.

Habchi, C., 2015. A gibbs energy relaxation (GERM) model for cavitation simulation. Atomization and Sprays 25,

Habchi, C., N. Dumont, O. Simonin, 2008. Multidimensional simulation of cavitating flows in diesel injectors by a homogeneous mixture modeling approach. Atomization and sprays 18,

Kapila, A., R. Menikoff, J. Bdzil, S. Son, D.S. Stewart, 2001. Two-phase modeling of deflagration-to-detonation transition in granular materials: Reduced equations. Physics of fluids 13, 3002-3024.

Kuijpers, M., D. Van Eck, M. Kemmere, J. Keurentjes, 2002. Cavitation-induced reactions in high-pressure carbon dioxide. Science 298, 1969-1971.

Kunz, R.F., D.A. Boger, D.R. Stinebring, T.S. Chyczewski, J.W. Lindau, H.J. Gibeling, S. Venkateswaran, T. Govindan, 2000. A preconditioned Navier–Stokes method for two-phase flows with application to cavitation prediction. Computers & Fluids 29, 849-875.

Kurschat, T., H. Chaves, G. Meier, 1992. Complete adiabatic evaporation of highly superheated liquid jets. Journal of Fluid Mechanics 236, 43-59.

Kwak, T., G. Mansoori, 1986. Van der Waals mixing rules for cubic equations of state. Applications for supercritical fluid extraction modelling. Chemical Engineering Science 41, 1303-1309.

Le Martelot, S., R. Saurel, B. Nkonga, 2014. Towards the direct numerical simulation of nucleate boiling flows. International Journal of Multiphase Flow 66, 62-78.

Le Métayer, O., R. Saurel, 2016. The Noble-Abel Stiffened-Gas equation of state. Physics of Fluids 28, 046102.

Linstrom, P.J., W. Mallard, 2001. NIST Chemistry webbook; NIST standard reference database No. 69.

Lund, H., 2012. A hierarchy of relaxation models for two-phase flow. SIAM Journal on Applied Mathematics 72, 1713-1741.

Ma, P.C., Y. Lv, M. Ihme, 2017. An entropy-stable hybrid scheme for simulations of transcritical real-fluid flows. Journal of Computational Physics 340, 330-357.

Matheis, J., S. Hickel, 2018. Multi-component vapor-liquid equilibrium model for LES of high-pressure fuel injection and application to ECN Spray A. International Journal of Multiphase Flow 99, 294-311.

Menikoff, R., B.J. Plohr, 1989. The Riemann problem for fluid flow of real materials. Reviews of modern physics 61, 75.

Menter, F.R., 1994. Two-equation eddy-viscosity turbulence models for engineering applications. AIAA journal 32, 1598-1605.

Michel, J., J. Franc, Fundamentals of cavitation. 2004, Springer.

Michelsen, M.L., 1982. The isothermal flash problem. Part I. Stability. Fluid Phase Equilibria 9, 1-19.

Moreau, J., O. Simonin, C. Habchi, 2004. A numerical study of cavitation influence on diesel jet atomisation. 19th annual meeting of the institute for liquid atomization and spray systems, Notthingham, England,

Murrone, A., H. Guillard, 2005. A five equation reduced model for compressible two phase flow problems. Journal of Computational Physics 202, 664-698.

Pantano, C., R. Saurel, T. Schmitt, 2017. An oscillation free shock-capturing method for compressible van der Waals supercritical fluid flows. Journal of Computational Physics 335, 780-811.

Patankar, S., 1980. Numerical heat transfer and fluid flow. CRC press.

Peng, D.-Y., D.B. Robinson, 1976. A new two-constant equation of state. Industrial & Engineering Chemistry Fundamentals 15, 59-64.

Perry, J.H., Chemical engineers' handbook. 1950, ACS Publications.

Petitpas, F., E. Franquet, R. Saurel, O. Le Metayer, 2007. A relaxation-projection method for compressible flows. Part II: Artificial heat exchanges for multiphase shocks. Journal of Computational Physics 225, 2214-2248.

Petitpas, F., J. Massoni, R. Saurel, E. Lapebie, L. Munier, 2009. Diffuse interface model for high speed cavitating underwater systems. International Journal of Multiphase Flow 35, 747-759.

Qiu, L., Y. Wang, Q. Jiao, H. Wang, R.D. Reitz, 2014. Development of a thermodynamically consistent, robust and efficient phase equilibrium solver and its validations. Fuel 115, 1-16.

Ransom, V.H., D.L. Hicks, 1984. Hyperbolic two-pressure models for two-phase flow. Journal of Computational Physics 53, 124-151.

Saha, S., J.J. Carrolls, 1997. The isoenergetic-isochoric flash. Fluid Phase Equilibria 138, 23-41.

Saurel, R., R. Abgrall, 1999. A multiphase Godunov method for compressible multifluid and multiphase flows. Journal of Computational Physics 150, 425-467.

Saurel, R., P. Boivin, O. Le Métayer, 2016. A general formulation for cavitating, boiling and evaporating flows. Computers & Fluids 128, 53-64.

Saurel, R., A. Chinnayya, Q. Carmouze, 2017. Modelling compressible dense and dilute two-phase flows. Physics of Fluids 29, 063301.

Saurel, R., F. Petitpas, R. Abgrall, 2008. Modelling phase transition in metastable liquids: application to cavitating and flashing flows. Journal of Fluid Mechanics 607, 313-350.

Saurel, R., F. Petitpas, R.A. Berry, 2009. Simple and efficient relaxation methods for interfaces separating compressible fluids, cavitating flows and shocks in multiphase mixtures. Journal of Computational Physics 228, 1678-1712.

Schmitt, T., L. Selle, B. Cuenot, T. Poinsot, 2009. Large-Eddy Simulation of transcritical flows. Comptes Rendus Mécanique 337, 528-538.

Segal, C., S. Polikhov, 2008. Subcritical to supercritical mixing. Physics of Fluids 20, 052101.

Simões-Moreira, J.R., 2000. Oblique evaporation waves. Shock waves 10, 229-234.

Simões-Moreira, J.R., J.E. Shepherd, 1999. Evaporation waves in superheated dodecane. Journal of Fluid Mechanics 382, 63-86.

Soave, G., 1972. Equilibrium constants from a modified Redlich-Kwong equation of state. Chemical Engineering Science 27, 1197-1203.

Tapriyal, D., R. Enick, M. McHugh, I. Gamwo, B. Morreale, High Temperature, high pressure equation of state density correlations and viscosity correlations. 2012, National Energy Technology Lab.(NETL), Pittsburgh, PA, and Morgantown, WV ….

Terashima, H., S. Kawai, M. Koshi, 2013. Consistent numerical diffusion terms for simulating compressible multicomponent flows. Computers & Fluids 88, 484-495.

Terashima, H., M. Koshi, 2012. Approach for simulating gas–liquid-like flows under supercritical pressures using a high-order central differencing scheme. Journal of Computational Physics 231, 6907-6923.

Thompson, P.A., H. Craves, G. Meier, Y.-G. Kim, H.-D. Speckmann, 1987. Wave splitting in a fluid of large heat capacity. Journal of Fluid Mechanics 185, 385-414.

Troshko, A., Y. Hassan, 2001. A two-equation turbulence model of turbulent bubbly flows. International Journal of Multiphase Flow 27, 1965-2000.

Utturkar, Y., J. Wu, G. Wang, W. Shyy, 2005. Recent progress in modeling of cryogenic cavitation for liquid rocket propulsion. Progress in Aerospace Sciences 41, 558-608.

Venkateswaran, S., J.W. Lindau, R.F. Kunz, C.L. Merkle, 2002. Computation of multiphase mixture flows with compressibility effects. Journal of Computational Physics 180, 54-77.

Vidal, J., 2003. Thermodynamics: Applications in chemical engineering and the petroleum industry. Editions Technip.

Wang, Y., L. Qiu, R.D. Reitz, R. Diwakar, 2014. Simulating cavitating liquid jets using a compressible and equilibrium two-phase flow solver. International Journal of Multiphase Flow 63, 52-67.

Wareing, C.J., R.M. Woolley, M. Fairweather, S.A. Falle, 2013. A composite equation of state for the modeling of sonic carbon dioxide jets in carbon capture and storage scenarios. AIChE Journal 59, 3928-3942.

Whitson, C.H., M.L. Michelsen, 1989. The negative flash. Fluid Phase Equilibria 53, 51-71.

Wilczek‑Vera, G., J.H. Vera, 2015. Understanding cubic equations of state: A search for the hidden clues of their success. AIChE Journal 61, 2824-2831.

Wood, A., 1930. A Textbook of Sound. 1930. G. Bell and Sons Ltd., London 23.

Yang, S., C. Habchi, P. Yi, R. Lugo, Towards a multicomponent real-fluid fully compressible two-phase flow model, in ICLASS 2018, 14th Triennial International Conference on Liquid Atomization and Spray Systems. 2018: Chicago, IL, USA.

Yang, S., Y. Li, X. Wang, U. Unnikrishnan, V. Yang, W. Sun, 2017. Comparison of tabulation and correlated dynamic evaluation of real fluid properties for supercritical mixing. 53rd AIAA/SAE/ASEE Joint Propulsion Conference,

Zein, A., M. Hantke, G. Warnecke, 2010. Modeling phase transition for compressible two-phase flows applied to metastable liquids. Journal of Computational Physics 229, 2964-2998.